SPIN DYNAMICS IN PRECISION MAGNETOMETRY

A THESIS SUBMITTED TO
THE GRADUATE SCHOOL OF ENGINEERING AND SCIENCE
OF BILKENT UNIVERSITY
IN PARTIAL FULFILLMENT OF THE REQUIREMENTS FOR
THE DEGREE OF
MASTER OF SCIENCE
IN
PHYSICS

By
Silvana Abi Mershed
December 2025

SPIN DYNAMICS IN PRECISION MAGNETOMETRY
By Silvana Abi Mershed
December 2025

We certify that we have read this thesis and that in our opinion it is fully adequate, in scope and in quality, as a thesis for the degree of Master of Science.

Deniz Aybaş(Advisor)

Ceyhun Bulutay

Alpan Bek

Approved for the Graduate School of Engineering and Science:

Orhan Arıkan
Director of the Graduate School

ABSTRACT

SPIN DYNAMICS IN PRECISION MAGNETOMETRY

Silvana Abi Mershed
M.S. in Physics
Advisor: Deniz Aybaş
December 2025

Spins constitute intrinsic quantum degrees of freedom whose behavior reflects fundamental interactions governed by their environments, making them sensitive indicators of magnetic fields across nuclear, atomic and solid-state platforms.

In Nuclear Magnetic Resonance (NMR), the nuclear spin ensemble is prepared and perturbed, then left to evolve until a signal is detected. Spectral broadening is analyzed with simulations showing that gradient-induced broadening for one-spin system can reproduce features commonly attributed to nuclear cross-relaxation in two-spin systems. Distinguishing between sources of spectral broadening motivates precision nuclear spin applications, including dark matter searches.

In alkali vapor systems, collective atomic spins are prepared and interrogated optically while enhancing coherence and signal quality using gases, coatings and temperature. The influence of gradients and quantum noise is examined in connection with high sensitivity measurements, exemplified by magnetoencephalography (MEG) and correlated searches for exotic physics using distributed networks such as GNOME (The Global Network of Optical Magnetometers to search for Exotic physics).

Nitrogen vacancy centers in diamond provide a solid-state setting in which electronic spins are initialized, driven, and readout through spin dependent fluorescence. In the sensing modalities studied, the roles of magnetic disorder, strain, and local spin baths are examined, together with applications in nanoscale NMR for biosensing applications and emerging dark matter sensing schemes.

Overall, the study highlights some of the factors that govern the behavior of spins across nuclear, atomic, and solid-state systems, clarifying the opportunities and limitations that define their use in precision magnetometry.

Keywords: Spin, Sensing, Magnetic Field Gradient, Spectral Broadening.

ÖZET

HASSAS MANYETİK ÖLÇÜMLERDE SPİN DİNAMİĞİ

Silvana Abi Mershed
Fizik, Yüksek Lisans
Tez Danışmanı: Deniz Aybaş
Aralık 2025

İçsel kuantum serbestlik derecelerini oluşturan spinlerin davranışları çevreleri tarafından yönetilen temel etkileşimleri yansıtır, ve bu da onları nükleer, atomik ve katı hal platformlarında manyetik alanların hassas göstergeleri haline getirir.

Nükleer Manyetik Rezonans'ta (NMR), nükleer spin topluluğu önce hazırlanır, sonra sarsılır, ardından da bir sinyal tespit edilene kadar evrimleşmeye bırakılır. Spektral genişleme, bir spin sistemi için gradyan kaynaklı genişlemenin, iki spin sisteminde nükleer çapraz gevşemeye dayandırılan özellikleri yeniden üretebileceğini gösteren simülasyonlarla analiz edilir. Spektral genişlemenin kaynakları arasında ayrım yapmak, karanlık madde aramaları da dahil olmak üzere hassas nükleer spin uygulamalarını motive eder.

Alkali buhar sistemlerinde, atomik spinler topluca hazırlanır ve gazlar, kaplamalar ve sıcaklık kullanılarak tutarlılık ve sinyal kalitesi artırılırken atomik spinler optik olarak sorgulanır. Gradyanların ve kuantum gürültüsünün etkisi, manyetoensefalografi (MEG), ve GNOME (Egzotik fiziği araştırmak için Küresel Optik Manyetometreler Ağı) gibi dağıtılmış ağlar kullanılarak egzotik fizik için korelasyonlu aramalarla örneklendirilen yüksek hassasiyetli ölçümlerle bağlantılı olarak incelenmiştir.

Elmas içindeki azot boşluk merkezleri, elektronik spinlerin başlatıldığı, yönlendirildiği ve spin asıllı floresans yoluyla okunduğu katı hal ortamı sağlar. İncelenen algılama yöntemlerinde, manyetik düzensizlik, gerilim ve yerel spin banyolarının rolleri, biyosensör uygulamaları ve ortaya çıkan karanlık madde algılama şemalarıyla nano ölçekli NMR uygulamaları birlikte incelenmiştir.

Genel olarak, çalışma, nükleer, atomik ve katı hal sistemlerinde spinlerin

davranışını yöneten bazı faktörleri vurgulayarak, hassas menyetik ölçümlerde kullanımlarını tanımlayan fırsatları ve sınırlamaları açıklığa kavuşturmaktadır.

Anahtar sözcükler: Spin, Algılama, Manyetik Alan Gradyan, Spektral Genişleme.

Acknowledgement

To my advisor, Deniz Aybaş, I couldn't have wished for a better mentor. Thank you for the countless Physics discussions, for the unwavering support, for challenging my thinking, and for creating a safe place when things around didn't feel so safe. Any clarity in this work is a testament to your guidance. You used to refer to me as the *Sisyphus of the Aybaş Lab* but this Sisyphus was indeed happy!

I am thankful that I have received a graduate student scholarship under my advisor's TÜBİTAK 2232-B International Young Researchers Program Grant number 122C341 with project title "Searching for new particles with laboratory-scale experiments using quantum magnetic sensors".

To the inspiring educators I have been fortunate of crossing paths with: Prof. Ceyhun Bulutay, whose courses, humbleness and kindness continue to teach me every day, Profs. Mehmet Özgür Oktel, Haitham Zaraket, Wissam Chemissany and Kassem Moghrabi whose quantum physics classes left me in absolute awe with every session, you made me fall in love with this field even more.

To my family, mom, dad, my sister Diana and my husband Ziad, the soul of my soul, my sanity and safe haven. Everything I do, is for you. Thank you for every sacrifice, seen and unseen. Mom and dad, you built for us a life overflowing with warmth and love, with memories of the funniest bed time stories, the best walks and talks and road trips with great songs. If I start thanking you I can never finish. Diana, the person who knows me from a glance, thank you for the loudest laughs of my life. Ziad, what have I done to deserve you?! You are the source of my $\varepsilon\acute{\upsilon}\delta\alpha\iota\mu o\nu\acute{\iota}\alpha$ and yes, as you say, this word bears the ultimate forms of love which I hold for you in my heart. Every page of this bears the invisible imprint of your extreme support.

To my friends, those who made the journey 100 times more fun. My friends from the Lebanese University, Imtithal, Mariana, Hadi and Mohammad Khaled, our meetings under our tree, our music, our books, our conversations and shared

silence are engraved in my memory in a very cherished way. My friends from Bilkent university, Burcu, Can, Efe, Yankı, Ahsen, Mohammad Hilal, Ahmed and Amna thank you for making this place feel like home, you have embraced me with lots of kindness and laughs. To my friend and office mate Nouha, I thank the person who made the decision of joining us in the same office every, single, day! Arkadaşlar, our shared breaks and anxieties, spontaneous conversations, and just the warmth of your presence turned this demanding journey into a very enjoyable one.

To my second family, my in-laws Ikhlas and Yasser, I have admired you way before Ziad, I have always admired your grace and kindness, thank you for all the love (and all the Zaatar), I am so blessed to have you in my life. My sisters and brothers in law and their amazing kids, being around you adds immense amounts of joy. I wish we are spatially closer but I am sure we will make it work.

Finally, to all my students and to that National Geographic photographer who I met only once in my life, your motivating words will always fuel my scientific research, thank you for leaving this beautiful impact.

Publications appearing in this Thesis

Part of Chapter 2 (texts and figures) will be submitted for publication as the following paper:

S. Abi Mershed, and D. Aybaş, "Growth in magnetic resonance spin response without the Overhauser effect", in preparation.

Contents

List of Figures

List of Tables

Chapter 1

Introduction

1.1 The Ubiquity of the Spin

Spin is the most familiar stranger in modern physics. While we measure, manipulate, polarize, and let them precess, we fail to describe spins or grasp them. On the atomic scale, a spin is not a motion through space but it is a built-in rythem for electrons and nuclei. A spin is said to be the *intrinsic* angular moment of a particle, thus it is a fundamental quantum property that lies at the heart of a scientific and technological revolution[5]. In nuclear magnetic resonance (NMR) and magnetic resonance imaging (MRI), nuclear spins reveal information about molecular structures and produce images of living tissues through their precession in magnetic fields [6, 7]. In optical magnetometers, electronic spins of alkali atoms in a vapor cell are manipulated to detect very weak magnetic fields that can allow us in looking for new fundamental physics [8]. In atomic clocks, the second is defined by the precise oscillations between spin states [9]. In solid state matter, single spins in color centers such as NV, SiV, GeV defects in diamonds act as nanoscale sensors [10] and in quantum information they serve as a qubit which is the unit of quantum memory and control used in quantum computing [11] and quantum network applications [12]. Thus, the spin, an invisible property, translates invisible fields into measurable signals allowing us to unfold many

secrets in physics, chemistry, biology, and medicine.

1.1.1 Magnetic Moments & Angular Momentum

At the heart of all the applications previously mentioned, lies a specific property of the spins that allows them to interact with or couple to the environment. Whether it is a nuclear or an electronic spin, the unifying element that interacts with external fields is the magnetic moment of the spin denoted by μ.

For electrons, in addition to the intrinsic spin angular momentum and since they are said to have orbital motion around the nucleus of the atom, they possess an *orbital* angular momentum. The spin angular momentum is characterized by the spin quantum number s which is a half-integer value of 1/2 for a single electron, while the orbital angular momentum is characterized by the orbital quantum number l. The total magnetic moment of the electron is

$$\begin{aligned} \boldsymbol{\mu_e} &= \boldsymbol{\mu_l} + \boldsymbol{\mu_s} \\ \boldsymbol{\mu_e} &= -g_l \mu_B \boldsymbol{l} - g_s \mu_B \boldsymbol{s} = -\mu_B (g_l \boldsymbol{l} + g_s \boldsymbol{s}) \\ \boldsymbol{\mu_e} &= -\mu_B (\boldsymbol{l} + 2\boldsymbol{s}) = -\frac{e\hbar}{2m_e c}(\boldsymbol{l} + 2\boldsymbol{s}) \end{aligned} \tag{1.1}$$

where e is the electronic charge, m_e is the electron's mass, c is the speed of light in vacuum, μ_B is known as Bohr's magneton and $\hbar$ is the reduced Planck's constant. For electrons, the magnetic moment is remarkably large due to its small mass, making electrons very sensitive to external fields.

For nuclei, their angular momentum is usually referred to as simply nuclear spin and it is denoted by I. The magnetic moment for the nuclear spin is:

$$\boldsymbol{\mu_I} = g_I \frac{e\hbar}{2m_p c} \boldsymbol{I} = g_I \mu_N \boldsymbol{I} \tag{1.2}$$

where g_I is the nuclear Landé factor, m_p is the proton's mass and μ_N is referred to as the nuclear magneton. Since μ_N is 2000 times smaller than μ_B, due to the ratio of proton and electron masses, the magnetic moment for the nuclear spins is much smaller than that for electronic spins and thus while electronic spins offer sensitivity, nuclear spins offer stability with their small magnetic moment [13].

In general, spin and magnetism are linked through a constant known as the gyromagnetic ratio and denoted by γ where $\gamma = \frac{e}{2m_e c}$ and thus:

$$\hat{\mu} = \gamma \hat{S}. \tag{1.3}$$

The gyromagnetic ratio is of great importance since, with the external magnetic field applied on the spins, their frequency of motion will be set as we will see later.

1.1.2 Spin Ensembles as a Probe

A spin ensemble refers to a large, statistically significant collection of quantum mechanical spins, whether nuclear or electronic spins. While a single spin behaves as a quantum two-level system, an ensemble of many spins can capture the collective behavior that emerges when these quantum entities interact with their environment. A spin ensemble responds collectively to external fields and the collective behavior gives rise to macroscopic observables like magnetization or changes in optical fields. What makes the spin ensemble so powerful as a probe is its dual nature: it embodies both the quantum coherence of individual spins and the statistical stability of a collective system, bridging the microscopic and macroscopic worlds. Through careful manipulation and control, these ensembles, can be made extremely sensitive to weak electromagnetic, mechanical or exotic fields as will be seen in this thesis.

1.2 Structure of the thesis

This thesis is organized into three main chapters, each examining a different spin-based quantum sensing platform and highlighting how spin dynamics, coherence and external interactions can shape their performance and applications.

Chapter 1 introduces the principles of nuclear magnetic resonance (NMR) as a foundational model for spin dynamics. It discusses spin polarization, coherent manipulation, relaxation mechanisms and readout, and examines how magnetic field gradients and spin interactions contribute to inhomogeneous broadening. The chapter also presents numerical simulations illustrating the interplay between gradient-induced broadening and the nuclear Overhauser effect, and concludes with an overview of NMR-based dark matter searches such as the CASPEr experiments.

Chapter 2 focuses on optically pumped magnetometers (OPMs), describing how optical pumping, probing, and atomic collisions produce high sensitivity atomic magnetometry. It analyzes the roles of buffer gases, anti-relaxation coatings, temperature control, and magnetic field gradients, as well as the technical and fundamental noise sources that limit sensitivity. The chapter highlights two applications of OPMs: magnetoencephalography (MEG) and global networks as GNOME that aim to detect correlated signals from exotic fields.

Chapter 3 examines nitrogen vacancy (NV) centers in diamond as a solid state quantum sensor platform. It discusses optical initialization, coherent microwave control, relaxation processes, and both cw-ODMR and pulsed-ODMR sensing modalities. The chapter reviews the origins and consequences of inhomogeneous broadening in NV ensembles and surveys applications in nanoscale NMR, biosensing, and emerging approaches for dark matter detection.

Finally, the **conclusion** synthesizes the insights gained across these platforms, emphasizing the unifying role of spin coherence and the diverse applications enabled by quantum sensing. It also outlines future directions, particularly the development of highly sensitive OPMs and of networked magnetometry and the

potential of quantum sensors in biomedical applications such as MEG.

Chapter 2

Nuclear Magnetic Resonance (NMR)

2.1 Spins' Journey in NMR

The collective dynamics of spin ensembles, find their most controlled and insightful realization in Nuclear Magnetic resonance (NMR). NMR is when nuclei, with non-zero spins, are prepared and then excited by magnetic fields, and the spin dynamics are turned later into measurable magnetic resonance signal . In this chapter, we will follow a spin ensemble's journey in NMR experiments specifically pulsed-NMR experiments. We will illustrate how the spin dynamics manifest as macroscopic observables and the spectrum that we get from perturbing them. The spectrum is usually a Lorentzian lineshape, however, in our work we noticed that the Lorentzian can be broadened and a two-peak structure can arise due to two distinct effects; the first is a gradient in the static magnetic field and the second is the nuclear Overhauser effect (NOE). Here, we will show how we were able to distinguish between the two origins of such a spectrum, which we referred to as the doublet structure. Analyzing and understanding the causes of such a spectrum will be of great help in enhancing the sensitivity of our precision experiments.

2.2 CW NMR vs. Pulsed NMR

Continuous-wave (CW) NMR represents the earliest era of magnetic resonance, pioneered in 1946 by *Felix Bloch* [14] and *Edward Purcell* [15] who first detected nuclear resonance by sweeping a continuous radio frequency field across the Larmor frequency. In CW-NMR, the RF amplitude is fixed and either the static magnetic field or the frequency is slowly scanned while monitoring absorption. The revolution in NMR came a few years later in the late 1950s with *Erwin Hahn's* discovery on spin echoes [16] which gave rise to pulsed NMR. Contrary to CW NMR, in pulsed NMR, short RF pulses perturb the spins and tip the magnetization of the ensemble then the full spin response is captured in the time domain as a free-induction decay which is transformed in the final steps to the frequency domain using Fourier transformation. Today, pulsed NMR dominates all chemical and biomedical applications due to its speed, sensitivity and ability to encode complex spin dynamics. Pulsed NMR will also be the workhorse of our study and simulations. Despite the success of pulsed NMR, CW NMR survives primarily in high-precision measurement like in dark matter detection experiments which will be discussed more in section 2.9.

2.3 NMR Setup

The essential components of an NMR experiment include the static magnetic field, the radio frequency (RF) excitation system, the sample and probe, and the detection system.

1. **Static Magnetic Field**
   A strong and homogeneous magnetic field B_0 splits the otherwise degenerate spin states and polarizes them along an axis referred to as the quantization axis (usually along z). High-resolution spectrometers use superconducting magnets. The magnets will be surrounded by liquid Helium and Nitrogen so that a magnetic field of several Tesla is reached [17].

2. **RF Excitation**
   A transverse oscillating magnetic field, produced by an RF coil and perpendicular to B_0, excites the spins when its frequency is close to the resonant frequency of the spin-splittings.

3. **Sample** & **Probe**
   The sample in the tube contains nuclei with non-zero spins. The tube is positioned at the center of the magnet where B_0 is uniform. The surrounding probe contains the RF coil used for both the excitation and the detection.

4. **Detection System**
   After the excitation pulse ends, the dynamics of the spins generates a time-varying magnetic flux in the detection coil which induces a voltage that forms the signal. The signal will be amplified, digitized and then transferred from the time to the frequency domain to get the NMR spectrum.

2.4 Spin Dynamics

2.4.0.1 Polarization

Substances are said to be magnetic if they are capable of interacting with magnetic fields. The interaction is only possible in the presence of a magnetic moment μ. Some magnetic materials are said to be permanent magnets meaning their μ is permanent like electrons, nuclei, bar magnets and compass needles and others are not permanent but their magnetism can be induced where their μ appears in the presence of an external magnetic field but is not always present [18]. The interaction between the magnetic moment and an external magnetic field was observed by *Pieter Zeeman* in 1896 where he experimented with a spectrum of sodium atoms in a magnetic field and observed broadening of spectral lines. This effect is currently known as the *Zeeman* effect.

In the quantum mechanical picture, the external magnetic field creates a splitting in the energy levels. The interaction Hamiltonian is:

$$H = -\boldsymbol{\mu} \cdot \mathbf{B}. \tag{2.1}$$

By solving the Hamiltonian, the eigenvalues give us the energy shifts which give us how much the atomic levels will be shifted under the effect of the magnetic field.

In the absence of an external magnetic field the spins are unpolarized, they are directed in random directions and the net magnetization that we are seeking and manipulating in spin ensembles, will be zero. For spins to be used as quantum sensors, first they need to be polarized, meaning, the spin ensemble should be driven out of a completely random orientation and should be prepared or set in a preferred alignment. Any interaction with any field that we are trying to sense or look for, will drive the spin ensemble away from the preferred alignment set ahead and from that non-equilibrium state, we can probe the interactions. Polarizing the spins in an NMR experiment happens by putting the sample in a static magnetic field B_0. Under a magnetic field B_0 directed along the z-axis, i.e. $\vec{B} = \hat{z}B_0$, the spins are in a state of thermal equilibrium, the lower energy state (aligned with B_0) is energetically favored. Since now spins will occupy the lower energy state, and since we have a collection of spins, we will deal with the net equilibrium magnetization M_0 which will be along the direction of the B_0 field.

Under an external magnetic field, the *spin's polarization*, the direction of the spin's angular momentum, responds to the field by moving *around* it. The motion of the magnetic moment of the spin around the field is called *precession*. Spins precess around the magnetic field or B_0-field with a frequency called the *Larmor* frequency and this frequency is actually set by $B_0$where it is denoted by ω_0 and:

$$\omega_0 = \gamma B_0. \tag{2.2}$$

2.4.0.2 Perturbation

What comes after polarization is a perturbation as known as RF excitation. Once polarized, the ensemble can be perturbed by an external alternating field such as a resonant radio RF field in the case of nuclear spins or microwave in the case of electron spins. This perturbative field, will set the spins in a state of non-equilibrium, it will drive transitions between the energy sublevels, tipping the magnetization vector away from equilibrium and causing the magnetization vector to precess around the static magnetic field.

In the classical picture, we focus on the dynamics of the spins and we study it through the differential equation of the angular momentum. In rotational motion, when an external torque is applied on an object that can rotate, a change in the angular momentum of the object will be induced. In electrons and nuclei, when a force is applied on the spins of these particles by a magnetic field, the force will create a torque and this will lead to a change in the spin angular momentum S. This can be described with the following differential equation:

$$\frac{d\vec{S}}{dt} = \vec{\tau} = \vec{\mu} \times \vec{B} = \gamma \vec{S} \times \vec{B} \tag{2.3}$$

The magnetization, when being away from its equilibrium position set by B_0, will try to relax back toward the state of thermal equilibrium. As it does that, the time evolution of this magnetization is studied as it encodes information about the system's structure or environment, couplings and its response to external fields. Thus, polarization serves as the initial condition and perturbation serves as the probe that allows us to extract the needed information from the ensemble.

2.4.0.3 Relaxation

Once perturbed, the ensemble does not remain indefinitely in its excited state. The ensemble gradually re-establishes thermal equilibrium through a process known as *relaxation*. This process is governed by two distinct time scales T_1

and T_2. The spin-lattice relaxation time constant or known also as the longitudinal relaxation time T_1, describes the recovery of population imbalance along the magnetic field direction. In the case of T_1, the lattice refers to the whole molecular framework surrounding the spins and their thermal motions. As a spin relaxes, it transitions from a state of high energy to a state of lower energy and as it does it releases this energy that is equal to its Zeeman splitting ($\Delta E = \hbar\omega_0$) to the lattice. As the lattice fluctuates, it can absorb energy from the spins or give energy to them. The longitudinal relaxation process is the net flow of energy from the excited spins back to the lattice until the Boltzmann ratio is restored. When the perturbative magnetic field is suddenly switched off, the longitudinal nuclear magnetization relaxes back to its equilibrium position M_0 following the formula:

$$\frac{dM_z}{dt} = \frac{-(M_z - M_0)}{T_1} \tag{2.4}$$

Since the longitudinal magnetization or M_z is parallel to the static field B_0, it will be static in the laboratory frame and thus it produces no time-varying magnetic flux, which means it cannot induce a voltage to be picked up by the receiver coil. To induce a detectable signal, the RF field should be applied perpendicular to the static field B_0. This RF field will exert a torque on the spins and will tip the magnetization towards the xy-plane. The resulting components are M_x and M_y, the transverse magnetizations. In the transverse plane, the transverse relaxation time T_2 describes the decay of phase coherence among spins precessing in the xy-plane. When a spin ensemble loses its phase coherence, we say its signal *dephases*. That is why T_2 is sometimes also referred to as the coherence decay time constant or dephasing time constant. While dephasing, the spins will be precessing at slightly different frequencies and that is because different spins in the ensemble experience slightly different magnetic fields, a case that is particularly interesting in our research. The transverse magnetizations after the RF pulse is switched off will change according to:

$$\frac{dM_x}{dt} = \frac{-M_x}{T_2} \tag{2.5}$$

$$\frac{dM_y}{dt} = \frac{-M_y}{T_2} \tag{2.6}$$

Minimizing relaxation and dephasing are central to extending coherence times, enhancing precision, and improving the performance of spin-based sensors and

quantum devices.

2.4.1 Bloch Equations

Polarization, perturbation by RF fields and relaxation can be incorporated phenomenologically into the Bloch equations [14], which describe how the magnetization evolves with time.

In the laboratory frame, where the magnetization is described with respect to fixed Cartesian axes, the Bloch equations take the form:

$$\frac{d\vec{M}}{dt} = \gamma\vec{M} \times \vec{B} - (\frac{M_x}{T_2}\hat{x} + \frac{M_y}{T_2}\hat{y} + \frac{M_z - M_0}{T_1}\hat{z}) \tag{2.7}$$

component wise:

$$\begin{aligned} \frac{dM_x}{dt} &= \gamma(M_y B_z - M_Z B_y) - \frac{M_x}{T_2} \\ \frac{dM_y}{dt} &= \gamma(M_z B_x - M_x B_z) - \frac{M_y}{T_2} \\ \frac{dM_z}{dt} &= \gamma(M_x B_y - M_y B_x) - \frac{M_z - M_0}{T_1}. \end{aligned} \tag{2.8}$$

In the lab frame, the RF field, oscillating at a frequency ω_{RF}, will introduce rapidly oscillating terms to the above equations which will make solving them a cumbersome task. To avoid the time-dependent terms from the oscillating RF field, we make our frame rotate at a frequency of $-\omega_{RF}$ and thus the oscillating field will look static. By doing this, we are moving from the lab frame to the rotating frame [19].

In the rotating frame, the magnetization $\tilde{M}(t)$ satisfies a modified Bloch equations in which the magnetic field B_z is now replaced with the effective magnetic field that accounts also for the rotation of the frame. The static magnetic field

originally contributes to a precession frequency ω_0 as in equation 2.2 and the frame itself rotates at ω_{RF} making the residual precession remaining in the rotating frame to be their difference which is called **detuning**:

$$\Delta\omega = \omega_0 - \omega_{RF} \tag{2.9}$$

The RF field should be perpendicular to the static magnetic field so the system can be either being driven on the x-axis or y-axis. In this work, driving along the y-axis is being done and so Bloch equations in the rotating frame with RF field on the y-axis will be shown in equation 2.10. However, the modified Bloch equations with RF field on the x-axis can be found in [6]. Following the same convention used in [6], $\Omega_e = -\gamma B_y$ which will give:

$$\begin{aligned}
\frac{d\tilde{M}_x}{dt} &= \Delta\omega\tilde{M}_y + \Omega_e M_z - \frac{\tilde{M}_x}{T_2} \\
\frac{d\tilde{M}_y}{dt} &= -\Delta\omega\tilde{M}_x - \frac{\tilde{M}_y}{T_2} \\
\frac{d\tilde{M}_z}{dt} &= -\Omega_e\tilde{M}_x - \frac{M_z - M_0}{T_1}
\end{aligned} \tag{2.10}$$

The equations can be solved numerically and then the transverse components M_x and M_y in the lab frame can be calculated using:

$$\begin{aligned}
M_x(t) &= \tilde{M}_x(t)\cos(\omega_0 t) - \tilde{M}_y(t)\sin(\omega_0 t) \\
M_y(t) &= \tilde{M}_x(t)\sin(\omega_0 t) + \tilde{M}_y(t)\cos(\omega_0 t)
\end{aligned} \tag{2.11}$$

which yields:

$$\begin{aligned}
M_x(t) &= M_0 e^{-t/T_2}\cos(\omega_0 t) \\
M_y(t) &= M_0 e^{-t/T_2}\sin(\omega_0 t)
\end{aligned} \tag{2.12}$$

where M_0 is the initial transverse magnitude.

2.4.2 Detection

Once the spin ensemble is polarized and interacts with external magnetic fields, its transverse dynamics manifest as a measurable signal. The fundamental principle of detection is Faraday's Law of Electromagnetic Induction. The change in magnetic field that happens while triggering the spins induces a current that can be detected by a nearby coil.

The oscillating electric current induced by the precession of the spins is called the free-induction decay or FID. The FID is the signal in the time-domain that contains all the information about the spin ensemble and its dynamics. The FID signal will show as an exponentially decaying oscillatory signal; showing a decaying cosine function for the transverse magnetization along the x-direction or M_x and a decaying sine function for the transverse magnetization along the y-direction or M_y. It is convenient to write the complex transverse magnetization as:

$$\begin{aligned} M_+(t) &= M_x(t) + iM_y(t) \\ M_+(t) &= M_0 e^{-t/T_2} e^{-i\omega_0 t}. \end{aligned} \tag{2.13}$$

The decay in the FID is caused by the relaxation of the spin ensemble and it is particularly interesting as it gives us information about the transverse relaxation time T_2. The shorter the transverse time T_2, the faster the spin ensemble relaxes and the more rapidly the signal decays.

The FID alone is not enough, to get information specifically about the frequency at which the spins are precessing, we need to go from the time domain to the frequency domain by doing a Fourier transformation to the FID signal. For the Fourier transform or FT we need to get a complex signal whose real and

imaginary parts are M_x and M_y respectively. That is because, if we rely on the M_x signal alone, and if we have a spin precessing in a clockwise direction and another in the counter clockwise direction ($+\omega_0$ and -ω_0), the cosine in M_x which is an even function, will not allow us to distinguish between the 2 precessions.

The one-sided FT of the FID is known as the *spectrum* and it is defined as:

$$\begin{aligned} S(\omega) &= \int_0^\infty M_+(t)e^{-i\omega t}dt \\ S(\omega) &= \int_0^\infty M_0 e^{-t/T_2}e^{-i\omega_0 t}e^{-i\omega t}dt \\ S(\omega) &= \frac{M_0}{\frac{1}{T_2} + i(\omega - \omega_0)} \end{aligned} \tag{2.14}$$

From equation 2.14, the real part of $S(\omega)$ gives the absorption spectrum and the imaginary part gives the dispersion spectrum. Since our signal is an exponentially decaying one, the line shape will be a *Lorentzian* whose resonance is centered at ω_0 and width is determined by T_2. For a small T_2 or a rapid relaxation, the line will be a broad one and as the relaxation is slower, the line is narrower [19].
In some systems, the detected spectrum can exhibit different shape than a Lorentzian where instead of a single narrow peak, we will get broadening, and that broadening can form multiple peaks. Such line shapes can reflect coherent interactions between coupled spins or distinct magnetic field environments.

2.5 Magnetic Field Gradients

In many NMR experiments, the applied static magnetic field is not perfectly uniform across the sample. Small spatial variations, known as static magnetic field gradients, arise naturally from imperfections in the main magnet, susceptibility differences between the sample and its container, or intentionally applied gradient coils. These gradients make the spins in our ensemble precess at slightly different

Larmor frequencies as seen in figure 2.1b, compared to how we want them to precess as seen in figure 2.1a which happens under a uniform static magnetic field. Instead of having $\omega_z = \omega_0 = \gamma B_0$, now our static magnetic field along the z-axis will be the combination of the original field and the gradients: $B_z = B_0 + Gz$ where G is the gradients and thus the frequency will be: $\omega_z = \omega_0 + \gamma G z$. As a result, the detected signal no longer originates from a single well-defined resonance frequency but from a distribution of frequencies, leading to characteristic inhomogeneous broadening for the NMR spectrum.

As each slice of the sample at position z precesses at a slightly different Larmor frequency, the local FID will be:

$$M_+(z,t) = M_0 e^{-t/T_2} e^{-i(\omega_0 + \gamma G z)t}. \tag{2.15}$$

To go from the local FID to the macroscopic FID, we integrate 2.15 over all positions so if we assume a 1D sample along z with length L where $-L/2 \leq z \leq L/2$ then our signal will not be a pure decaying exponential anymore, but an exponential multiplied with a spatial interference factor, reflecting phase dispersion induced by the gradients as shown in equation 2.16.

$$\begin{aligned} M_+(t) &= M_0 e^{-t/T_2} e^{-i\omega_0 t} \int_{-L/2}^{L/2} e^{-i\gamma G z t} dz \\ M_+(t) &= M_0 e^{-t/T_2} e^{-i\omega_0 t} \left\{ \frac{2\sin(\gamma G L t/2)}{\gamma G t} \right\}. \end{aligned} \tag{2.16}$$

In the frequency domain, the spectrum with the gradient is the Fourier transform of the above FID:

$$S(\omega) = \int_0^{\infty} \int_{-L/2}^{L/2} M_0 e^{-t/T_2} e^{-i(\omega_z - \omega)t} dz\, dt$$

$$S(\omega) = \int_{-L/2}^{L/2} M_0 \frac{1}{\frac{1}{T_2} + i(\omega_0 + \gamma G z - \omega)} dz \tag{2.17}$$

$$S(\omega) = \frac{M_0}{i\gamma G} \ln\left(\frac{\frac{1}{T_2} + i(\omega_0 + \frac{\gamma G L}{2} - \omega)}{\frac{1}{T_2} + i(\omega_0 - \frac{\gamma G L}{2} - \omega)} \right) \tag{2.18}$$

The above expression clearly shows that without gradient, $\omega_z = \omega_0$ and a single Lorentzian is recovered but with a gradient, different positions will give different resonance frequencies ω_z so the observed spectrum is a superposition of Lorentzians and the result is an inhomogeneously broadened line shape.

Unwanted magnetic field gradients that cause inhomogeneous broadening can be corrected through shimming. After measuring the distorted line shape, small compensating magnetic fields are applied and iteratively adjusted to make B_0 as uniform as possible across the sample volume. By progressively minimizing the linewidth and restoring the Lorentzian, shimming effectively reduces dephasing between spins and recovers high spectral resolution.

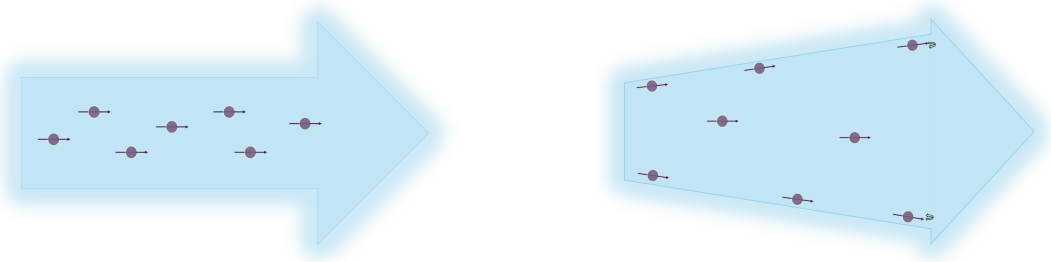

(a) (b)

Figure 2.1: Comparison between an ensemble of spins under a homogeneous magnetic field (a) and an ensemble under a spatially varying field, where the gradient induces differences in local Larmor frequencies (b).

2.6 Nuclear Overhauser Effect (NOE)

In addition to the basic dynamics described earlier by the Bloch equations, NMR systems often contain interactions that modify the time evolution of the magnetization. Among these interactions, one of the richest ones is the dipole-dipole interaction which couples the angular momenta of nearby nuclear spins. This interaction not only shifts the energy levels and modifies relaxation rates, but also enables cross-relaxation between spins giving rise to the **Nuclear Overhauser Effect** or **NOE**.

In his original proposal, Overhauser observed that saturating the conduction electron spin in a metal changes the polarization of the nuclear spin [20]. In NOE, a nuclear spin (instead of the electron) is irradiated, and the resonance lines of a spatially close (but spectrally far) nuclear spin are observed. NOE was experimentally demonstrated by Solomon who measured a doublet of an HF molecule [21], and this experiment is known as "Double Resonance" [22]. Solomon also incorporated dipolar cross-relaxation into Bloch equations. NOE can be thought of as a "ruler" that measures inter-nuclear distances, making it indispensable in determining molecular structures and in probing molecular dynamics [6], [23].

In NMR, as spins are polarized under a static magnetic B_0 and then perturbed with RF field B_{RF}, the following interactions can be presented with the following total Hamiltonian:

$$H(t) = \underbrace{-\gamma_I \hbar (B_0 + B_{\text{grad}}) I_z}_{H_0} + \underbrace{-\gamma_I \hbar B_{\text{RF}} (I_y \sin \omega t)}_{H_{\text{RF}}(t)} \tag{2.19}$$

where γ_I is the gyromagnetic ratio of spin I and I_y and I_z are the projections of the nuclear spin of spin I on the y-axis and the z-axis respectively.

In the presence of NOE, we will have in addition to spin I which its interactions

are shown in the above Hamiltonian, another spin sample to be referred to as spin S. Spin S will also be polarized so it will be affected by H_0 but it will not be resonantly irradiated so no H_{RF} interaction term goes to spin S. In the presence of a dipole-dipole interaction between spins I and S, Hamiltonian H_{DD} will be added to equation (2.19) to show how spins I and S will be coupled. H_{DD} is given by:

$$H_{\mathrm{DD}} = \frac{\mu_0}{4\pi} \frac{\gamma_I \gamma_S \hbar^2}{r^3} \Big[\vec{I} \cdot \vec{S} \; - \; 3 \left(\vec{I} \cdot \hat{r}\right) \left(\vec{S} \cdot \hat{r}\right) \Big] \tag{2.20}$$

with γ_I and γ_S are the gyromagnetic ratios of spins I and S respectively, r is the internuclear distance between the 2 spins, $\hat{r}$ is the unit vector along the internuclear distance. The presence of r and $\hat{r}$ in the Hamiltonian, tells us that this coupling is anisotropic, depending on both the distance between the spins and the orientation of $\hat{r}$ relative to the spin operators.

To understand what NOE is, a pair of spin-1/2 nuclei will be used as a simple example so the focus will be only NOE and no quadrupole interactions. The pair of spin-1/2 nuclei under a static magnetic field will form a four-energy Zeeman sublevel system so that the four unperturbed eigenstates can be represented as $|++\rangle$, $|+-\rangle$, $|-+\rangle$ and $|--\rangle$. In the absence of coupling between the spins, each spin relaxes independently through single quantum transitions, W_1, as represented in diagram 2.2 with the arrows in green color. The dipolar Hamiltonian in equation 2.20, introduces two additional transitions; zero-quantum transitions connecting $|+-\rangle$ and $|-+\rangle$, represented by W_0 and the red arrow, and double-quantum transitions connecting $|++\rangle$ and $|--\rangle$, represented by W_2 and the yellow arrow. W_0 transition is referred to as flip-flop and W_2 transition is referred to as flip-flip. Details about the calculation of the transition probabilities, W_0, W_1 and W_2 will not be shown here but can be found in [21].

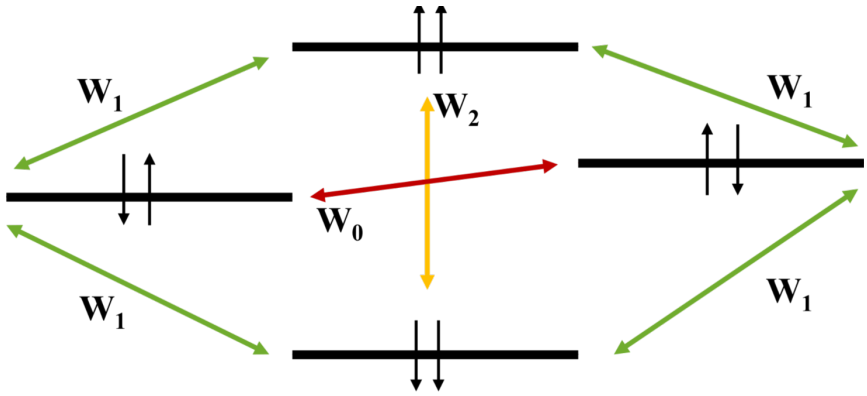

Figure 2.2: Energy level system of two spin-1/2 nuclei under Nuclear Overhauser Effect

In the two-spin system, and for simplicity the spins will be referred to as spins I and S and the NOE dynamics are represented in figure 2.3. Initially, the two spins will be prepared with spin S in the $+S_z$ state and spin I is inverted, such misalignment is needed to observe NOE. Then spin I will be irradiated with a hard pulse. The altered populations of spin I feed into the dipolar-allowed pathways and drive a redistribution of populations for both spins until they finally relax back to their equilibrium magnetization.

This population redistribution within the four-level Zeeman energy diagram constitutes the microscopic origin of the NOE, and the macroscopic evolution of the longitudinal magnetizations resulting from these coupled population flows is described quantitatively by the Solomon cross-relaxation equations.

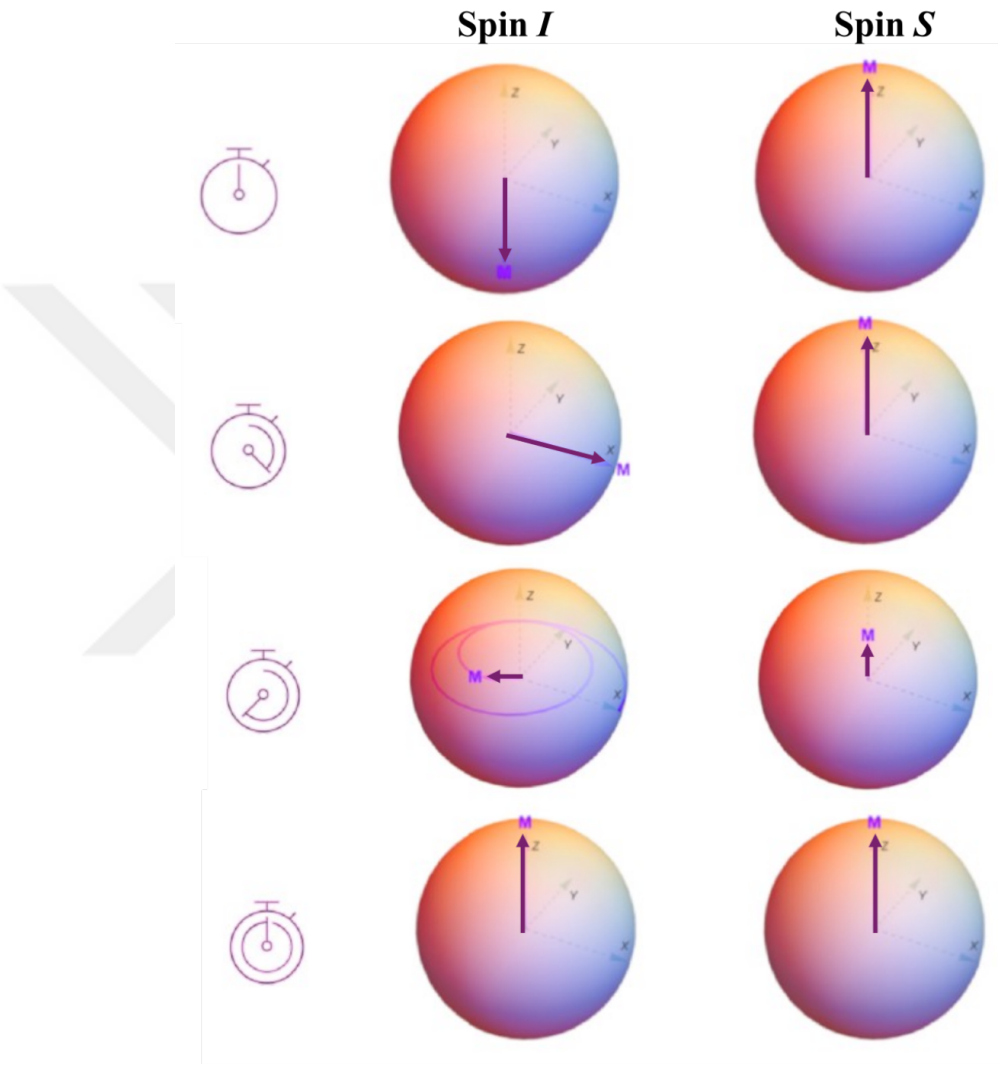

Figure 2.3: A schematic showing spin dynamics under NOE where the Bloch spheres on the left represent the spin being perturbed, spin I, and the Bloch spheres on the right represent spin S, the spin which is unperturbed by external fields but is affected by the dynamics of spin I due to coupling to it.

The Bloch equations introduced before will now be modified by adding another set of equations to describe the dynamics of spin S and by incorporating the cross-relaxation constant σ in the longitudinal magnetization. In the new set of equations, instead of representing the magnetization by M, it will be represented by I and S to distinguish between the magnetizations of both spins.

$$\begin{aligned}
\frac{d\tilde{I}_x}{dt} &= \Delta\omega\tilde{I}_y, + \Omega_e I_z - \frac{\tilde{I}_x}{T_{2I}} \\
\frac{d\tilde{I}_y}{dt} &= -\Delta\omega\tilde{I}_x - \frac{\tilde{I}_y}{T_{2I}}, \\
\frac{dI_z}{dt} &= -\Omega_e\tilde{I}_x - \frac{I_z - I_0}{T_{1I}} - \sigma(\tilde{S}_z - \tilde{S}_0), \\
\frac{d\tilde{S}_x}{dt} &= \Delta\omega\tilde{S}_y - \frac{\tilde{S}_x}{T_{2S}}, \\
\frac{d\tilde{S}_y}{dt} &= -\Delta\omega\tilde{S}_x - \frac{\tilde{S}_y}{T_{2S}}, \\
\frac{dS_z}{dt} &= -\frac{S_z - S_0}{T_{1S}} - \sigma(\tilde{I}_z - \tilde{I}_0)
\end{aligned} \tag{2.21}$$

.

The longitudinal relaxation time and the coherence time of spin I are respectively T_{1I} and T_{2I} and the longitudinal relaxation time and the coherence time of spin S are respectively T_{1S} and T_{2S}.

This sigma term is inversely proportional to r_{IS}^6 where r_{IS} is the distance between the nuclei I and S, so the closer the nuclei are to each other, the more pronounced the Nuclear Overhauser effect. The equation for sigma is [24]:

$$\sigma = \frac{\tau_c}{10} K^2 \left[\frac{6}{1 + (\omega_I + \omega_S)^2\tau_c^2} - \frac{1}{1 + (\omega_I - \omega_S)^2\tau_c^2} \right] \tag{2.22}$$

with

$$K = \frac{\gamma_I \gamma_S \hbar}{r_{IS}^3} \left(\frac{\mu_0}{4\pi} \right) \tag{2.23}$$

In the previous equation, γ_I and γ_S are the gyromagnetic ratios of I and S

respectively, ω_I and ω_S are the Larmor frequencies of I and S respectively, and τ_c is the rotational correlation time of the molecule.

For fast tumbling molecules, their very fast orientation means that τ_c is short and as τ_c decreases, σ increases. If we think about a very simple case where the molecule has identical atoms, meaning $\omega_I = \omega_S = \omega$, if the molecule is fast tumbling this will make $\omega\tau_c \ll 1.12$, which will give a $\sigma > 0$ and thus we will have a positive NOE enhancement which means as we irradiate one of the spins, spin I for instance, we will get an increase in the signal intensity of the other spin or spin S.

However, in the case of slow tumbling molecules, which reorient slowly, τ_c is large which will make σ smaller in value. Not only σ will be small, but also if we go back to the simple example of the same atom molecule, we will see that in slow tumbling molecules, $\omega\tau_c \gg 1.12$ and this will make $\sigma < 0$ which, upon irradiation of spin I, there will be decrease in the signal of spin S and this is the negative NOE enhancement [25].

2.7 J-coupling

In addition to the above interactions, there is another one worth mentioning to clear any confusion. Since in this work the focus will be on the signals that arise from pulsed NMR with and without NOE, and since some of these signals have a doublet-like structure, one should be careful not to confuse these doublet-like structures with the ones that arise from J-coupling. In the case of J-coupling, the doublet-like structure is caused by scalar spin-spin coupling that is mediated via the chemical bond in molecules, this happens when the electron wavefunction has a non-vanishing value at the position of the nucleus which will cause the nuclear magnetic moments to affect each other through the electronic cloud [6]. The J-coupling between two spins, I and S can be represented by the Hamiltonian $H_J = \hbar J\, \mathbf{I} \cdot \mathbf{S}$, where J is the scalar spin-spin coupling constant. When such a coupling is present, the resonant lines of spins I and S acquires a multiplet

structure and in the simplest case of spin-1/2 nuclei, the resulting splitting is a doublet with equal intensities if other couplings or relaxation imbalances are ignored. J-coupling is seen more in liquids because of the fact that the fast tumbling in liquids can mask or average out some effects like the dipole-dipole interaction, that leads to line broadening which makes the J-coupling harder to be resolved. Unlike J-coupling, the NOE does not generate the doublet-like structure, meaning it does not generate the splitting, however, it modifies the intensities of the splitting. Thus, the doublet-like structure observed in under NOE, should be inherently unequal in intensities since they reflect a redistribution of population. In our case, the J-coupling will be ignored but the doublet-like structure that is arising even though J-coupling is not considered will be explained later.

2.8 Simulations

In an effort to distinguish between line shape broadening caused only by magnetic field gradients, or caused by magnetic field gradients in the presence of NOE, simulations were carried out.

In this work, we initially simulated using Bloch equations one type (spin I) of non-interacting nuclear spins under magnetic drive with detuning around resonance. Then, we simulated using Solomon equations adding a second type (spin S) under the same conditions, except for coupling I and S through NOE.

In our simulations, the systems are initially prepared such that spin I is inverted by a π-pulse from the direction set by B_0, while spin S is in thermal equilibrium along B_0. This preparation is crucial for observing NOE, which arises from cross-relaxation pathways that transfer polarization between the two spins. This transfer becomes detectable when the longitudinal polarizations of I and S are maximally misaligned relative to one another. Inverting spin I creates this non-equilibrium condition. Spin S, kept in the $+S_z$ state, acts as the "responder spin". Its longitudinal magnetization S_z responds to the magnetic perturbation

applied to spin I through its coupling to I_z.

After polarizing both spins in this manner, a total of 20 consecutive $\pi/2$-pulses are applied to spin I, while monitoring its dynamics in the following three cases:

Case 1: Zero interaction with a spin S (using Bloch equations)

Case 2: Non-zero interaction with spin S (using Solomon equations)

Case 3: Non-zero interaction with spin S under zero magnetic gradient (using Solomon equations)

For each case, we ran simulations in three regimes where spin-lattice relaxation times of spins I and S are varied with respect to the wait time between consecutive pulses.

In the simulation, some of the parameters were held constant and they will be shown in table 2.1. While others, like the relaxation times and the cross-relaxation constant σ, were varied based on each regime and will be shown in the respective regime. Here, γ is the gyromagnetic ratio of spin I, B_0 is the static magnetic field, B_{grad} is the gradient in the static magnetic field and it is only present in the first 2 cases, B_{RF} is the RF magnetic field, N_{spins} is the number of spins simulated, N_{pulses} is the number of pulses given to spin I, t_{pulse} is the pulse duration, t_{wait} is the waiting time between the beginning of consecutive pulses and $\theta_{tipping}$ is the tipping angle from the magnetization set by B_0 which is along the z-axis.

2.8.1 First Regime: Slow Relaxation

In this case study, the longitudinal relaxation times of both spins I and S were set relatively larger than t_{wait} which is the waiting time set between the start of consecutive pulses.

Table 2.1: Fixed Parameters in the Simulation

Parameter	**Magnitude**
γ	2π (1/s·T)
B_0	1 T
B_{grad}, if present	10% of B_0
B_{RF}	12.5 mT
N_{spins}	301
N_{pulses}	20
t_{pulse}	20 s
t_{wait}	300 s
$\theta_{tipping}$	$\pi/2$

Table 2.2: Slow Relaxation Regime Parameters

Parameters	**Magnitude**
Longitudinal relaxation time of spin I T_1 (s)	3000
Transverse relaxation time of spin I T_2 (s)	40
Longitudinal relaxation time of spin S T_1 (s)	2000
Transverse relaxation time of spin S T_2 (s)	10
Dipole-dipole cross relaxation constant $\sigma_{\mathrm{IS}}\,(s^{-1})$	0.0004

While doing that, the spins will not be allowed to have a full recovery to their equilibrium positions before the next pulse. In this regime, the saturation regime, the successive pulses will keep on saturating the spins.

First, we plotted the deviation of the longitudinal magnetizations from equilibrium for both the Bloch case and the Solomon case, both of which are with gradient in the static magnetic field. In figure 2.4a, we can see that all the curves are still far from zero as the system evolves and that is understandable because we deliberately chose the T_1 relaxation time to be so long thus not allowing the system to have enough time to relax back to equilibrium between the pulses. The blue curve which shows the dynamics and deviation of the longitudinal magnetization of spin I in the Bloch case, recovers faster than the orange curve because in the Bloch model, spin I relaxes only through its own relaxation time T_{1I}. In

the Solomon case however, cross-relaxation transfers part of the of $I's$ longitudinal polarization towards spin S, effectively providing an additional relaxation pathway that slows the return of I_z toward equilibrium this is why the orange curve is not approaching equilibrium as fast as the blue curve. In the pure Bloch description, spin S is completely decoupled from the dynamics of I since we never drive S and we don't couple it to I and without the coupling, its magnetization simply stays at its thermal value which is zero. By contrast, in the Solomon case, the same cross-relaxation terms that slow down spin I, simultaneously drive spin S away from equilibrium, building up the positive deviation shown by the green curve; this is the signature of NOE, the transfer of polarization from the inverted spin I to the spin it is coupling to which is S.

Plotting the longitudinal magnetization dynamics in figure 2.4a was helpful to assure that our spins are performing in the expected manner. Next, we wanted to observe the transverse magnetization and see if there will be any difference mainly between the Bloch case and Solomon case with magnetic field gradient, but we also plotted that of Solomon without magnetic field gradient to assure that the only thing causing the broadening and doublet structure is the gradient and nothing related to NOE.

In this regime, where the longitudinal relaxation times are much longer than t_{wait}, the spin enssemble has very little time to repolarize along z between consecutive pulses. After the initial inversion and the first few excitation pulses, the available longitudinal polarization I_z is gradually used up, so each pulse, beyond the first pulse, will be only tipping part of the remaining I_z into the transverse plane, creating an FID and thus a contribution to PSD. With almost no recovery or just a partial recovery, the magnitude of I_z available to be tipped gets smaller from pulse to pulse. Since the transverse signal is affected by the longitudinal component, a lack of recovery for I_z will only mean a decaying overall PSD as the system is driven towards saturation. That is why in all the 3 plots of figure 2.5 we are seeing a decreasing PSD with increasing pulse number. The later increase in figure 2.5a in the Bloch case is particularly interesting and will be discussed shortly.

The change in spectra between the cases where there is gradient in the magnetic field (figures 2.5a and 2.5b) and where the gradient is nulled (figure 2.5c) is of high interest in our work. Specifically, the cause behind the broadening that we see in figures 2.5a and 2.5b where at some or almost all pulses, we are seeing a very broadened spectra up to the point of observing a clear two-peak (doublet) structure. This structure is a direct consequence of the static field gradient B_{grad} as when B_{grad} was removed in figure 2.5c, the one-peak Lorentzian line shape was recovered. Understanding how B_{grad} causes a doublet is crucial but first we need to recall that the static magnetic field B_0 is what sets the Larmor frequency in an NMR experiment. In the presence of a gradient in the field, the spins will be affected by a continuous distribution of resonance frequencies rather than a single frequency. Spins will be feeling a different magnetic field and thus will be precessing at slightly different rates. In the time domain, their transverse components accumulate different phases and some parts of the sample will become in-phase while others will be out-of-phase with respect to the reference. When we Fourier transform the FID to obtain the PSD, the constructive interference (in-phase parts of the sample) and the destructive interference (out-of-phase parts of the sample) will give the structure we see. Instead of one Lorentzian peak we obtain a split line with the double-peaked spectra being the fingerprint of the gradient-induced phase dispersion across the ensemble.

After establishing that the double-peaked spectra is fully and solely related to the gradient in the field, we noticed that, after a few pulses, a different trend will also arise between Bloch and Solomon (figures 2.5a and 2.5b). Although both cases start with a strong PSD that then decays because of the long T_1 saturation discussed above, their long-time behavior is different. In the Bloch model (figure 2.5a), spin I as mentioned before relaxes through its own T_1 and nothing else. Recall that initially spin I is strongly inverted for reasons that support NOE. The first few repeated pulses deplete the inverted polarization and push I_z toward zero (towards the xy-plane) with I_z being small, tipping it into the transverse plane yields little M_x and thus decreasing the PSD. Over long times, however, the slow T_{1I} relaxation begins to rebuild a positive equilibrium magnetization towards $+I_z^0$. Once I_z has crossed the xy-plane and started to grow towards its thermal

value, each pulse again has more longitudinal magnetization to act on. As a result, the PSD amplitude increases again. this gives the characteristic "max $\rightarrow$ dip $\rightarrow$ partial recovery" behavior seen in the Bloch case. As for the Solomon case (figure 2.5b), because of the coupling between spins I and S and because spin S is acting as an additional relaxation channel to spin I, the cross-relaxation will continually leak the polarization away into S_z. Consequently, the amount of longitudinal polarization available for excitation never recovers enough to boost M_x again. Each new pulse finds I slightly more depleted and more "shared" with S. That is why, the net effect is a monotonic decrease of the PSD amplitude with pulse number.

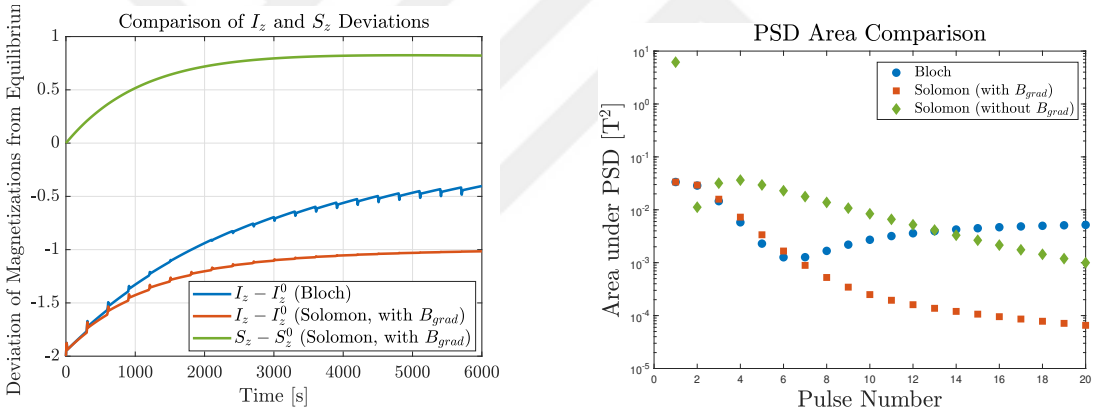

(a) (b)

Figure 2.4: Plots showing (a) the deviation of longitudinal magnetization from equilibrium versus time for the two cases with magnetic field gradient (Bloch and Solomon) and (b) the area under the PSD of the transverse magnetization versus pulse number for the 3 cases.

The signal amplitudes of the observed magnetization in this case is expected to decrease after each pulse.

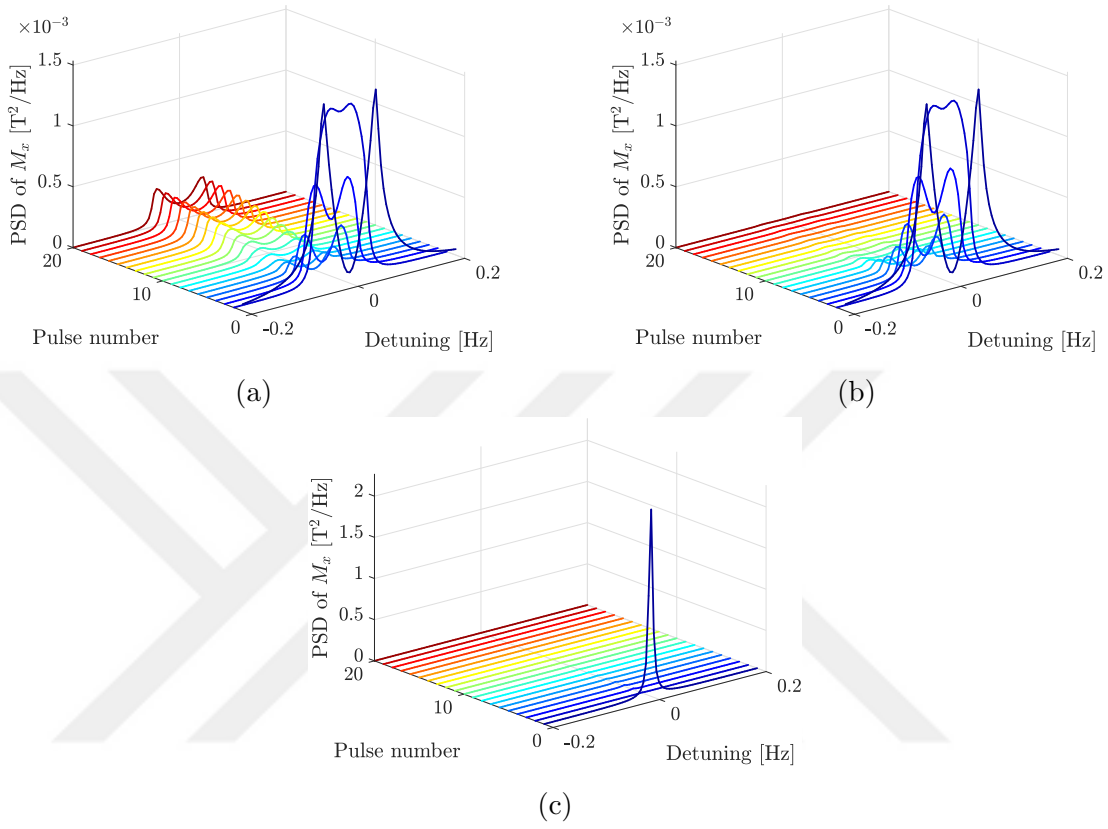

Figure 2.5: Power Spectral Density of M_x transverse magnetization of spin I versus pulse number versus detuning in (a) Bloch case with gradient in the magnetic field, (b) Solomon case with gradient in the magnetic field and (c) Solomon case but without gradient in the magnetic field.

To complement the detailed PSD plots in figure 2.5, we also plot the area under each spectrum as a function of pulse number as shown in figure 2.4b. This scalar observable compresses all spectral details into a global, physical, measurable quantity which allows a clear comparison between models (Bloch vs. Solomon) and between physical mechanisms (cross-relaxation vs. gradients). In the Bloch case the area exhibits a characteristic decrease followed by a partial recovery, reflecting the competition between pulse-induced saturation and T_1 repolarization. In contrast, the Solomon dynamics with a gradient produce a strictly monotonic decay demonstrating that cross-relaxation and gradient-enhanced dephasing remove transverse power fast. Without a gradient, Solomon dynamics yield a much

larger initial spectral power followed by a rapid collapse, isolating the spin-spin coupling. Therefore, this plot reveals all the dynamical behaviors that cannot be easily obvious from the PSD plots alone and as separate as they are.

2.8.2 Second Regime: Fast Relaxation

In the second case study, the longitudinal relaxation times of both spins I and S were set relatively shorter than the waiting time between the pulses. In this case, the longitudinal magnetizations behave in a fundamentally different manner from the first case.

Table 2.3: Fast Relaxation Regime Parameters

Parameters	**Magnitude**
Longitudinal relaxation time of spin I T_1 (s)	30
Transverse relaxation time of spin I T_2 (s)	40
Longitudinal relaxation time of spin S T_1 (s)	20
Transverse relaxation time of spin S T_2 (s)	10
Dipole-dipole cross relaxation constant $\sigma_{\mathrm{IS}}\,(s^{-1})$	0.04

As seen in figure 2.6a, the blue trend depicting spin I in the Bloch case is rapidly going back to equilibrium after each pulse. The Solomon dynamics also exhibit a rapid recovery for spin I but it is slower than the Bloch case due to polarization exchange with spin S as explained earlier. The most characteristic feature of this regime is the response of spin S where in the early part of the sequence, the perturbation of spin I drives a buildup in polarization in S through cross-relaxation, producing the initial rise in the green curve. However, as the rate of relaxation is fast it over takes the rate of polarization transfer, making S_z quickly drawn back toward equilibrium.

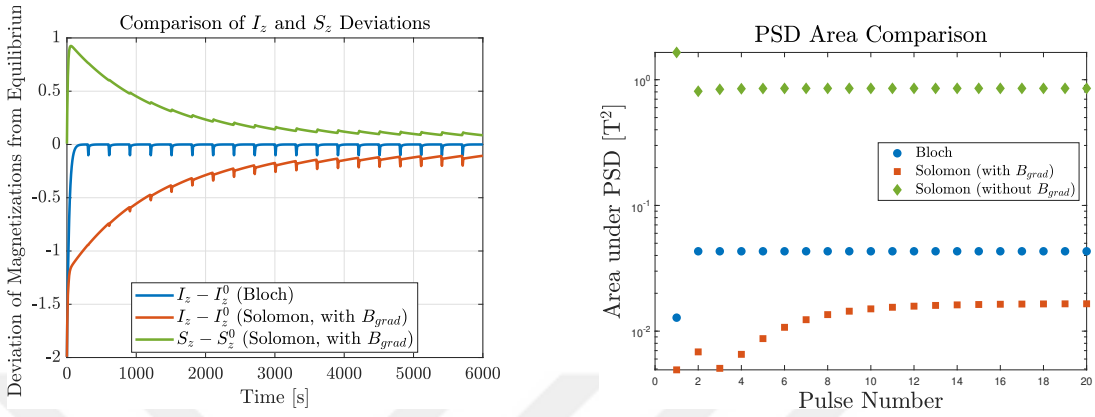

(a) (b)

Figure 2.6: Plots showing (a) the deviation of longitudinal magnetization from equilibrium versus time for the two cases with magnetic field gradient (Bloch and Solomon) and (b) the area under the PSD of the transverse magnetization versus pulse number for the 3 cases.

In this fast relaxation regime, the PSD evolution as can be observed, differs a lot from the previous regime. In the Bloch case, figure 2.7a, and after the first pulse, the transverse magnetization spectrum exhibits a three-peak structure consisting of a broadened central peak and two smaller symmetric peaks. The central peak is located at the Larmor frequency of the ensemble (i.e. zero detuning in the rotating frame) and originates from a short-lived, phase coherent transverse magnetization that is created when the longitudinal magnetization of spin I was initially polarized and then coherently rotated by the first pulse. The two smaller peaks appearing symmetrically on either side of the central peak are located at positive and negative detuning frequencies and arise from spins whose local Larmor frequencies are shifted by the gradient, corresponding to ensembles precessing at detuned frequencies. Following the first pulse, the gradient in the magnetic field continuously imprints phase dispersion, causing the transverse magnetization generated in subsequent pulses to be distributed among detuned spatial modes rather than forming a globally phase aligned spin response (central peak). The fast T_1 relaxation restores the longitudinal magnetization as seen from the blue trend in 2.6a but in the presence of inhomogeneities, phase uniformity is not restored, a condition required to regenerate the central coherent

peak. Because of the fast relaxation, the PSD amplitude directly saturates in this regime as equilibrium is always getting re-achieved, unlike the first regime.

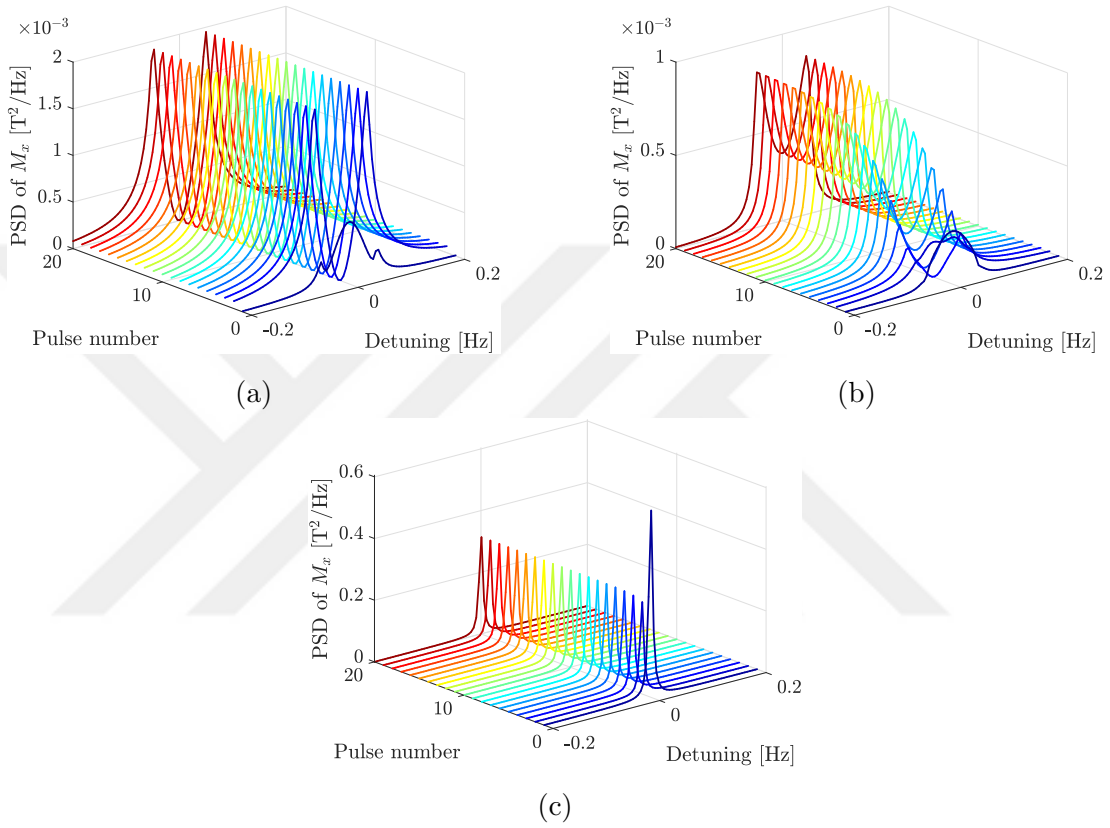

Figure 2.7: Power Spectral Density of M_x transverse magnetization of spin I versus pulse number versus detuning in (a) Bloch case with gradient in the magnetic field, (b) Solomon case with gradient in the magnetic field and (c) Solomon case but without gradient in the magnetic field.

It is so important to explain here why the central peak structure was never seen in the PSD of the Bloch case in the first regime but it is obvious in this regime. The reason goes back to the transverse relaxation time or the coherence time T_2 which describes how long the spins remain phase coherent in the transverse plane after they are tipped by the RF field. In the first regime, T_2 is much shorter than the longitudinal relaxation T_1 which means that the longitudinal magnetization recovers very slowly and the transverse magnetization loses coherence very quickly. As a result, any transverse signal created by the pulse decays before a

strong well-defined peak can form at the central frequency due to the fast loss of coherence. Thus, the absence of a central peak in the first regime, reflects the fact that short T_2 suppresses coherent transverse contributions. In this regime, since T_2 is comparable to T_1, a coherent transverse contribution is observed but directly destructed by the continuously imprinted phase dispersion.

In the Solomon case, the evolution of the power spectral density reflects, in addition to relaxation and gradient effects, a gradual exchange of longitudinal magnetization between spins I and S through NOE. After the first two pulses, the coupled system produces a broad central blob as seen in 2.7b, with increased area under the PSD during the second pulse as seen in the orange trend in figure 2.6. This increase in the area is caused by the increased broadening that is related to gradient effects kicking in along with cross-relaxation effects. By the third pulse, cross-relaxation has started to redistribute magnetizations and with the gradient imprinting more phase dispersion, the central blob has disappeared and a well-defined two-peak structure has evolved with a reduced total area. In subsequent pulses, the system does not immediately saturate, instead, the amplitude and the total area of the two-peak spectrum increase gradually from pulse to pulse. Unlike the Bloch case where longitudinal magnetization of spin I rapidly returns to equilibrium after each pulse, the Solomon equations describe a coupled system in which the longitudinal magnetization of spin I builds up progressively.

In the Solomon case without a magnetic field gradient, figure 2.7c, the first RF pulse converts the maximum available longitudinal magnetization of spin I into a strong transverse signal that survives for a long time due to the long coherence time T_2. Again in this case, in the absence of gradients, a Lorentzian line shape takes place and this idea was emphasized earlier. After the first pulse that produces a maximum PSD, Solomon cross-relaxation transfers part of the longitudinal magnetization from spin I to spin S so less spin I magnetization is available for subsequent pulses. In the absence of any inhomogeneities and dephasing effects, and in the presence of the long coherence time, the transverse channel will remain highly efficient, so each later pulse will produce a smaller transverse signal since less longitudinal magnetization is getting recovered for perturbation. This causes the PSD to decrease and then saturate as a steady

balance is reached. In contrast when a magnetic field gradient is present, it causes spins at different positions to precess at different Larmor frequencies, leading to rapid loss of phase alignment between their transverse components and thus suppressing the ensemble's transverse coherence even when the intrinsic T_2 is long and that is why in the Bloch and Solomon cases with gradient in this regime, the longitudinal magnetizations recovered back to equilibrium and produced an increasing PSD rather than a decreasing one in the absence of gradient.

Again here the area under the PSD plot, figure 2.6b shows a compact illustration of the transverse magnetization that each pulse is able to generate. The Bloch case and Solomon without gradient case spin dynamics were observed easily from the their PSD plots. However, in the Solomon with gradient case, understanding the dynamics especially after the first few pulses was clearer through the area plot as was explained earlier.

2.8.3 Third Regime: Mixed Relaxation

For completeness, the mixed relaxation regime was also examined. In this regime, the longitudinal relaxation time of spin I was chosen to be much larger than t_{wait} but the longitudinal relaxation time of spin S was chosen shorter. This configuration is common in heteronuclear NMR.

Table 2.4: Mixed Relaxation Regime Parameters

Parameters	**Magnitude**
Longitudinal relaxation time of spin I T_1 (s)	3000
Transverse relaxation time of spin I T_2 (s)	40
Longitudinal relaxation time of spin S T_1 (s)	200
Transverse relaxation time of spin S T_2 (s)	10
Dipole-dipole cross relaxation constant $\sigma_{\mathrm{IS}}\,(s^{-1})$	0.0004

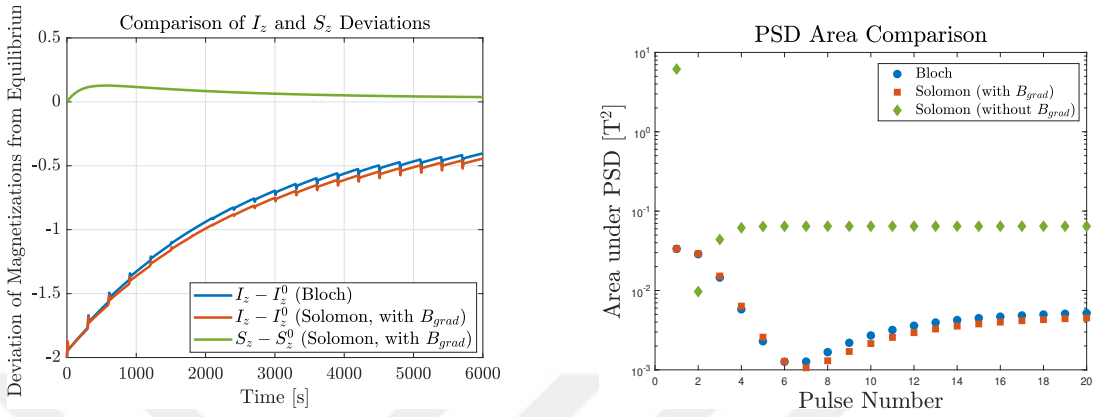

(a) (b)

Figure 2.8: Plots showing (a) the deviation of longitudinal magnetization from equilibrium versus time for the two cases with magnetic field gradient (Bloch and Solomon) and (b) the area under the PSD of the transverse magnetization versus pulse number for the 3 cases.

Here, spin I behaves as it did in the first regime (slow-relaxation regime), whereas spin S, with its fast relaxation, is preventing NOE buildup. In this case, the blue curve in figure 2.8a referring to the Bloch case shows a slow recovery of spin I, whose longitudinal magnetization remains far from equilibrium over the full pulse train. The same dynamics of spin I in the Bloch case were observed in figure 2.4a which is expected since the only difference now is T_{1S} which has no effect on Bloch. Spin I in the Solomon case behaves so similar to that in the Bloch case, while spin S has a small initial rise in the green curve followed by a rapid decay. The small difference between the blue and the orange curves with just the slight change in the green curve, reflects the weak polarization leakage from I into the coupled spin S.

With nearly no changes in the PSD plots for the Bloch case and the Solomon case without gradient between the first and this regime, the Solomon with gradient (figure 2.9b) behaves so differently from the first regime (figure 2.5b). In this regime, the transverse spectra of the Bloch and the Solomon with magnetic field gradients become nearly identical. This is totally understandable because spin S with its rapid relaxation, loses any polarization, preventing the NOE signature

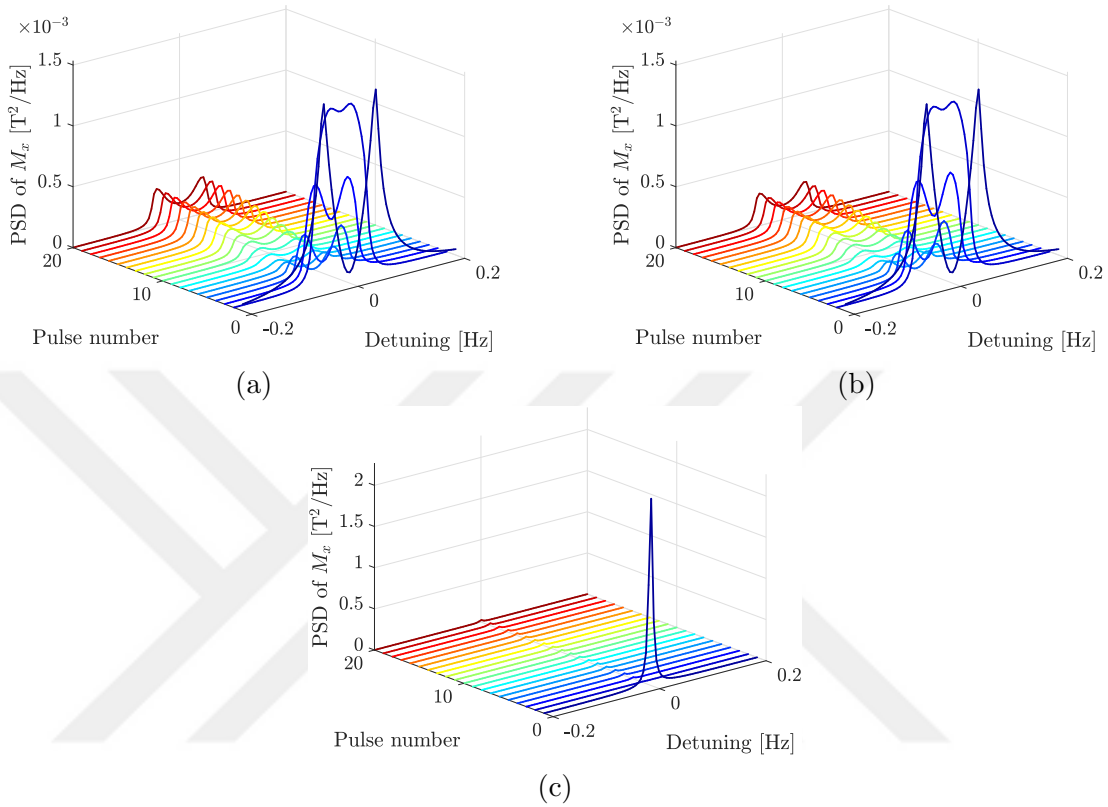

Figure 2.9: Power Spectral Density of M_x transverse magnetization of spin I versus pulse number versus detuning in (a) Bloch case with gradient in the magnetic field, (b) Solomon case with gradient in the magnetic field and (c) Solomon case but without gradient in the magnetic field.

resulting in spin I behaving as an isolated spin.

The compact representation in the Area under the PSD, figure 2.8, shows that the cases where gradients are present are clearly distinguishable from the case where there is absence of gradient (green diamonds). However, as was also seen in the PSD plots, Bloch with gradients and Solomon with gradients are indistinguishable especially initially. With consecutive pulses, a minuscule difference appears where Bloch's case area is slightly higher than Solomon's area. The reason for Solomon with gradients area being less, is explained in this case, and all previous cases, to be caused by the coupling between the two spins by NOE.

2.8.4 Summary of Results

The above simulation results showed the evolution of pulsed NMR spectra using Bloch and Solomon formalisms to clarify how magnetic-field gradients, relaxation times and the nuclear Overhauser effects shape spectral features beyond the ideal Lorentzian limit. In the absence of gradients, a single-spin Bloch system exhibits the expected Lorentzian line shape arising from homogeneous transverse relaxation. When a magnetic field gradient is present, spins at different spatial positions experience different local magnetic fields and therefore precess at different Larmor frequencies, leading to an inhomogeneous dephasing and a modification of the spectrum. This frequency dispersion broadens the line and produces a two-peak structure rather than a single Lorentzian. Extending the analysis to two-spin systems under NOE and governed by the Solomon equations shows that NOE-induced cross-relaxation can further modify the pulse to pulse spectral evolution, although in some regimes the resulting spectra remain difficult to distinguish from single-spin Bloch dynamics. By comparing slow, fast, and mixed relaxation regimes, the roles of the relaxation times T_1 and T_2 in determining the shape and evolution of the spectrum were highlighted. Overall, these results emphasize that pulsed NMR spectra are governed by the combined effects of field inhomogeneities, relaxation, and spin-spin coupling and the non-Lorentzian line shapes originate from field gradients but they get altered differently under mechanisms like NOE.

2.9 Hunting Axions with NMR

The Standard model of particle physics represents our most comprehensive framework for describing fundamental particles and three of the four fundamental interactions. However, this very successful model has been "stained" by one of the most baffling problems in Quantum Chromodynamics (QCD), which is the strong CP problem of QCD. Helen Quinn and Roberto Peccei proposed a solution to this problem in 1977 and that solution is Axion Physics. First proposed as a

solution to the strong CP problem, the axion later also became a dark matter candidate. The axion is a light and weakly interacting hypothetical particle but there has been many intensive research going on to try to detect it. NMR is one of the experimental setups that tries to look for these elusive signals.

2.9.1 The Strong CP Problem

The strong CP problem is commonly expressed as the failure to observe a permanent electric dipole moment (EDM) for the neutron [26]. To understand this more, we should dive a bit deeper into the Lagrangian of QCD. In the QCD Lagrangian, we have a term that permits CP violation and that is the θ term:

$$\mathcal{L}_\theta = \theta \, \frac{\alpha_s}{8\pi} \, G^a_{\mu\nu} \, \tilde{G}^{a\,\mu\nu} \tag{2.24}$$

where $G^a_{\mu\nu}$ is the gluon field strength tensor, a indicates the eight gluon color charges and α_s is the gluon's field coupling constant [27]. The Gluon field tensor, analogues to the Faraday tensor [28], violates CP symmetry just as $E \cdot B$ violates it where $E \cdot B$ is odd under P- and T-symmetry but even under C-symmetry which makes it CP violating. The θ parameter in the QCD Lagrangian, is associated with the QCD vacuum state where the QCD has many degenerate vacua and the physical vacuum is a θ-weighted superposition of them [29, 30]. Any value of this θ that is different from zero, introduces CP-violation in the strong interaction. Not only that, but also, theoretically, the neutron's EDM is proposed as $|d_n| \sim 10^{-16}\, \bar{\theta}_{\mathrm{QCD}}$ e.cm $\sim 10^{-16}$ e.cm, however, experimentally it is found to be $|d_n| \sim 1.8$ x 10^{-26} e.cm [26]. As a solution, Peccei and Quinn [31, 32, 33, 34] proposed $\bar{\theta}_{\mathrm{QCD}}$ to be a *dynamical variable* that can become naturally small and as it relaxes to zero, it solves the CP problem in the Lagrangian. The Peccei-Quinn mechanism introduces a spontaneously broken symmetry, giving rise to the bosonic axion whose field dynamically relaxes $\bar{\theta}_{\mathrm{QCD}}$.

2.9.2 Dark Matter & Axions

Modern cosmology rests on the realization that the luminous matter we observe accounts only for a small fraction of the universe's total mass-energy count. There are significant clues for the existence of dark matter which will be presented here along with discussing why the axion can be a dark matter candidate. Early investigations of stellar dynamics in the Milky Way provided the first clues about dark matter by comparing luminous and total galactic mass, revealing that stellar matter dominates in the local solar neighborhood [35]. Subsequent work on the Coma Cluster uncovered a discrepancy between the measured velocity dispersion of galaxies and the value predicted by the observed luminous mass [36, 37]. This provided early evidence that dark matter dominates over visible matter on cluster scales. Later discoveries of hot gas in galaxy clusters reduced, but did not eliminate the discrepancy. Further evidence for dark matter comes from galactic rotation curves, which were found to remain flat well beyond the radius enclosing most of the luminous matter [38, 39, 40]. This behavior indicates that galactic mass distributions are dominated by extended, roughly spherical dark matter halos extending far beyond the visible components of galaxies. Gravitational lensing provides further compelling evidence for dark matter, as the bending of light by gravity allows the underlying mass distribution to be inferred from image distortions [41]. Studies of merging galaxy clusters using lensing [42] revealed that, while baryonic matter interacts and slows during collisions, the dominant mass component passes through largely unaffected and this non-baryonic matter is referred to as dark matter. Another key observational signature pointing to dark matter is the power spectrum of the Cosmic Microwave Background (CMB). The subtle temperature variations in the CMB arise from acoustic oscillations in the coupled photon-baryon plasma in the early universe [43]. The relative positions and heights of the acoustic peaks are highly sensitive to the amount and nature of matter present at recombination. Cosmological fits to the CMB power spectrum show that baryonic matter alone cannot reproduce the observed peak structure [44]. The data requires a matter that cannot interact with radiation and remains dynamically cold at recombination and some of the peaks in the power spectrum of the CMB that are not related to the baryonic content, tell us the amount of

dark matter compared to regular matter and light and that was a very strong evidence.

While dark matter is still a mystery, its nature is one of its biggest mysteries. There are so many theories about the nature of dark matter and so many experiments trying to look for the dark matter candidate which can span over a huge range of mass. Here, the focus will be on the axion, an ultra-light bosonic dark matter (UBDM) which is a boson whose mass $\ll 10$ eV and that is why it is referred to as ultralight [27]. Thus, the axion is a solution to the strong CP-problem as discussed in the previous section and is a dark matter candidate, that is why searching for it is so important and has been an active area of research.

2.9.3 Detecting Axions

The axion is a spinless, chargeless, ultra-light hypothetical particle so its detection is not straightforward. To try to detect axions or axion-like particles (ALPs), first we need to understand the couplings that they can make with baryonic matter and we have three couplings:

1. **Axion-Photon coupling:** with interaction Hamiltonian $H \sim a\mathbf{E}\cdot\mathbf{B}$, where a is the axion field, E the electric field and B the magnetic field of the photon
2. **Axion-Gradient or Axion-Nucleon coupling:** with interaction Hamiltonian $H \sim \boldsymbol{\sigma} \cdot \boldsymbol{\nabla a}$, where σ is the spin of the nucleon and ∇a is the gradient of the axion field
3. **Axion-Gluon coupling:** with interaction Hamiltonian $H \sim a\boldsymbol{\sigma} \cdot \mathbf{E}$, where E is an applied electric field which will be explained later

In this work, the focus will be on the axion-gradient coupling and the axion-gluon coupling and the experiments that try to look for axions under these couplings are the CASPEr-Wind and CASPEr-Electric, respectively. CASPEr or

Cosmic Axion Spin Precession Experiment is an NMR experiment seeking to find axions or ALPs.

2.9.3.1 CASPEr-Wind

Is a haloscope experiment that searches within the Milky Way's dark matter halo for ALPs. This experiment uses the idea that the motion of Earth through the galaxy leads to a relative velocity between it and the dark matter. The interaction that this experiment relies on is $H = g_{aNN}\,\boldsymbol{\sigma} \cdot \boldsymbol{\nabla a}$, where g_{aNN} is the coupling strength between the ALP wind and the nucleons. The coupling between the nucleons and the ALP dark matter "wind", will make the nucleons' spins precess around the local direction of the ALP's momentum ∇a as long as they are not aligned [45]. The axion field is approximated as $a \sim a_0 \cos(m_a t)$ where m_a is the axion mass, therefore the axion nucleon coupling will become $H = g_{aNN}\, m_a\, a_0 \cos(m_a t)\, \mathbf{v} \cdot \boldsymbol{\sigma}$, where $v \sim 10^{-3}\, c$ is the velocity of the Earth relative to the galactic ALPs. This perturbation causes a small and time-varying energy shift.

Since the experiment used in this detection uses NMR, a sample of nuclear spins will be polarized and the polarization should not be aligned with the relative velocity $\vec{v}$ between the Earth and the dark matter [46]. In NMR, the resonant spin precession will be caused by an RF coil that induces an RF magnetic field oscillating close to the Larmor frequency. However, in CASPEr-Wind, there is no RF coil and the resonant spin precession of the nucleons will be induced by "axion wind" which can be thought of as an oscillating pseudo-magnetic field and thus the coupling can be represented as $H \sim \mathbf{B} \cdot \boldsymbol{\sigma}$. The experimental protocol used here is specifically continuous wave NMR or CW-NMR. In CW-NMR, the RF magnetic field is not applied in pulses, but rather it is applied continuously and frequencies are probed by alternating the static magnetic field magnitude or the oscillating magnetic field frequency. Since we do not know the frequency of ALP and since the ALP wind is continuous then CW-NMR is an ideal experiment to look for these elusive signals [47]. The experiment is operated and signals are probed until a resonance is detected through a Lorentzian signal. The Lorentzian

will take place at the Larmor frequency which is in this case the ALP's frequency ($\omega_L = \omega_a = \gamma\,|B_0|$).

In this NMR protocol, and since it is used to look for very faint signals, avoiding signal broadening is very crucial since signal broadening can reduce the sensitivity. To avoid the broadening which is caused, as discussed, by gradient in the static magnetic field B_0, B_0 should be spatially homogeneous and that is achieved by using superconducting NMR magnets that will induce a B_0 field of about 20 T. With this, using CASPEr-Wind, ALPs with frequency ranging between few Hz - 100 MHz ($m_a \sim 10^{-14} - 10^{-6} eV$) can be detected.

2.9.3.2 CASPEr-Electric

CASPEr-Electric looks for axion particles through the axion-gluon coupling. The EDM interaction probed by this experiment depends on the coupling of axions to the gluon field [48]. The Hamiltonian in this case will be $H = g_d\, a\, \boldsymbol{\sigma} \cdot \boldsymbol{E^*}$ where g_d is the coupling strength and E^* is an effective Electric field [49]. As mentioned before in the strong CP-problem, since the neutron's EDM is related to θ_{QCD}, as $|d_n| \sim 10^{-16}\,\bar{\theta}_{\mathrm{QCD}}$ and the axion field is proportional to the θ-term $a(t) \propto \bar{\theta}_{\mathrm{QCD}}$, then it is possible to look for axions by looking for the neutron's EDM instead. To do that, in CASPEr-Electric, NMR was used to look for this EDM with some tweaking. The spins first were polarized under a strong static magnetic field as in all NMR experiments. However, instead of perturbing the spins with an oscillating magnetic field, a static electric field applied perpendicular to B_0 was applied to target the EDM. To look for axion signals, as in CASPEr-Wind, B_0 was tuned to scan for resonance [49]. The coupling between the axions and gluons is expected to induce an oscillating EDM of the form:

$$d_n = g_d\,\frac{\sqrt{2\rho_{\mathrm{DM}}}}{\omega_a}\cos(\omega_a t) \tag{2.25}$$

where ρ_{DM} is the local dark matter density and m_a is the axion mass. The interaction between the oscillating EDM at frequency m_a and the static E-field will make the spins precess, thus inducing an effective magnetic field that can

be probed. When the axion-induced EDM oscillates at the Larmor frequency ($\omega_L = \omega_a = \gamma B_0$), resonance will be reached and from that Lorentzian peak we can infer ω_a. Under this experiment and EDM coupling, similar frequency range to that in CASPEr-Wind can be scanned for the axion.

The pickup probe (or detection coil) in an NMR system converts the precessing transverse magnetization of the nuclear spins into an induced voltage through Faraday's law. The experimental observable in CASPEr-Electric is the oscillating transverse magnetization: $M_a = u\, M_0\, \Omega_a\, T_2\, \cos(\omega_a\, t)$, where M_0 is the equilibrium magnetization of the sample's nuclear spin, Ω_a is the Rabi frequency which quantifies the magnitude of the torque, T_2 is the nuclear spins' coherence time and u is a dimensionless spectral factor that accounts for inhomogeneous broadening and detunings between the ALP Compton frequency and the Larmor frequency [1]. Because the induced voltage in an NMR output depends not only on the sample magnetization M but also on the coil geometry and other electronics, the raw output signal is not directly proportional to the actual magnetization of the spin ensemble. Calibration is therefore essential to relate the measured voltage to the absolute magnetization. A calibrated probe allows us to determine the static magnetic field B_0, the longitudinal and transverse relaxation times T_1 and T_2, and Rabi frequency. If these values were quantified, the Larmor frequency can be accurately inferred. In precision experiments including low-field NMR and axion searches such as CASPEr, a well-calibrated pick-up coil is crucial as the targeted signals will be extremely weak, where even small uncertainties in coil sensitivity could mimic or obscure a physical signal.

In the CASPEr-Electric experiment using solid-state NMR carried out by Aybas et al. (2021), ALPs were being looked for using $^{207}Pb^{2+}$ ions with nuclear spin $I = 1/2$, in a poled ferroelectric PMN-PT crystal. The pickup coil was calibrated using ^{207}Pb pulsed-NMR measurements. The spins were excited by resonant magnetic field pulses and after each pulse FID was measured with a pickup probe [1]. After the FID was taken, Fourier transform was performed for the detected voltage signal and the spectral density versus frequency plots were obtained for three different excitation-pulse lengths values $t_p = 0.2$, 2 and 20 ms. Data of T_1 and T_2 values were extracted. The plots shown below 2.10,

show rather than a Lorentzian, a broadened signal with plots for $t_p = 0.2$ and 2 ms showing obvious doublet structure caused by inhomogeneous broadening [1]. This broadening in the spectrum for the ^{207}Pb solid-state NMR was consistent with the chemical shift anisotropy (CSA) of ^{207}Pb observed in solid-state NMR [50]. Broadening in the spectra can help us extract the gradient in B_0 and account for it so that the correct Larmor frequency is analyzed and the sensitivity is enhanced.

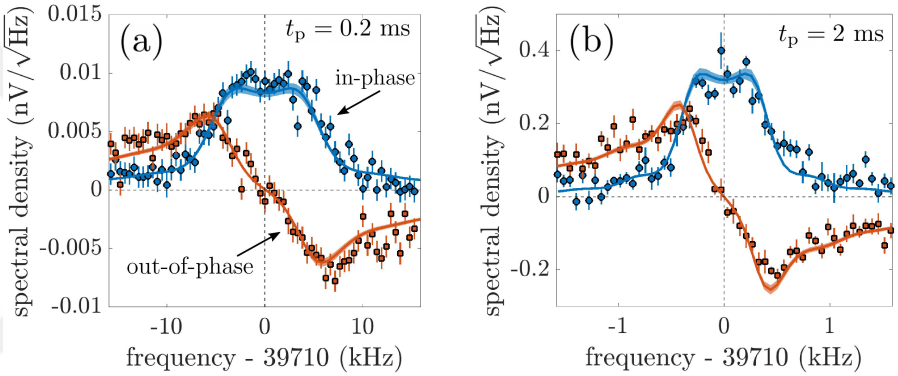

Figure 2.10: Schematic from the CASPEr-Electric experiment, specifically from the caliberation of the solid-state NMR experiment which shows broadening in the spectrum [1]. Adapted from Aybas *et al.*, "Search for Axionlike Dark Matter Using Solid-State Nuclear Magnetic Resonance," *Phys. Rev. Lett.* **126**, 141802 (2021), https://doi.org/10.1103/PhysRevLett.126.141802. Licensed under the Creative Commons Attribution 4.0 International License (CC BY 4.0).

2.9.3.3 CASPEr-ZULF

In CASPEr-Wind & Electric, SQUIDs are used as ultra-sensitive magnetic field detectors (pickup sensors) that read the tiny transverse magnetization induced by the nuclear spins. In both CASPEr experiments, the minimum frequency that can be detected is $\sim$ few Hz but below that frequency, the experiment will not be sensitive anymore. That is because of the **$1/f$ knee frequency** (also called the flicker-noise corner frequency) which is the frequency below which the noise in a detector stops being flat or white noise and begins to rise as $1/f$ [51]. Meaning, that the noise amplitude grows as the frequency decreases so if we want to detect a frequency lower than a few Hz, we will stumble upon the **$1/f$ knee frequency**

constraint in SQUID magnetometers. Above the knee frequency, typically at frequencies of several Hertz, the SQUID achieves its optimal sensitivity , limited primarily by thermal and amplifier noise, yielding a stable noise floor. However, at frequencies below the knee, a variety of slow noise processes begin to dominate.

In the search of axions and ALPs below ~ 10 Hz, a non-resonant measurement protocol can be used and it could be implemented as a low-frequency extension to CASPEr [47], thus overcoming the sensitivity problem of SQUIDs. The need to scan for resonance will be removed and the appearance of sidebands will be caused by the modulation of the Larmor frequency. Sidebands here are actually helpful and needed in the detection of axions and ALPs. A third CASPEr experiment is proposed for this objective and it is CASPEr-ZULF where ZULF refers to Zero-to Ultra-Low-Field. ZULF is a type of NMR experiment that operates in the regime of zero to microtesla magnetic fields, where the Zeeman interaction is weaker than or comparable to nuclear spin-spin interactions (J-couplings) [52].

In CASPEr-ZULF, instead of detecting axion-induced resonance at a Larmor frequency $\omega_L = \gamma B_0$, axion-induced effects on **J-couplings** in nuclear spins is looked for. In CASPEr-ZULF, the coupling of the axion or ALP to nucleons is also used with some tweaking where the interaction Hamiltonian is:

$$H = \hbar J_{CH}\, \mathbf{I}\cdot\mathbf{S} \;-\; \hbar(\gamma_H \mathbf{I} + \gamma_C \mathbf{S})\cdot\mathbf{B} \;+\; \hbar\left(g_{app}\,\mathbf{I} - \frac{1}{3} g_{ann}\,\mathbf{S}\right)\cdot \mathbf{D}_{\text{wind}}(t) \quad (2.26)$$

where a two-spin system will be used and J_{CH} is the electron-mediated spin-spin coupling, I and S are the nuclear spin operators for our atoms of interest in the sample which are ^{1}H and ^{13}C, γ_H and γ_C are the gyromagnetic ratios of ^{1}H and ^{13}C spins respectively, the applied magnetic field is denoted by B, the coupling strengths g_{app} and g_{ann} are for the ALP-proton and ALP-neutron coupling respectively which are considered the same and can be instead denoted by g_{aNN} or the ALP-nucleon coupling strength, and D_{wind} is the axion wind which is ∇a. [2]. In the case of the chosen sample in this experiment by Garcon *et al.* (2019), both ^{1}H and ^{13}C have a nuclear spin of 1/2 ($I = S = 1/2$) and thus the total nuclear spin F is going to have a singlet and a triplet manifold. The allowed selection rules here are $\Delta F = 0, \pm 1$ and $\Delta m_F = 0, \pm 1$. In the absence of external fields where $B = D_{wind} = 0$, the triplet state $F = 1$ is degenerate

and $F = 0$ is separated from $F = 1$ with $\hbar J_{CH}$. This will lead to a zero-field spectrum that consists of a Lorentzian as seen in figure 2.11**A**. However, if a magnetic field is to be applied along the z-direction, it will lift the degeneracy from the $F = 1$ state without affecting the $F = 0$ state. When the degeneracy is lifted, two peaks will appear instead of the single Lorentzian as shown in figure 2.11**B**. There is a need to clarify that the static magnetic field B is the above Hamiltonian is not the same as the magnetic field used in polarizing the spins. In fact, in ZULF NMR experiments, the spins are polarized first in a strong magnetic field (1-3 T) and then rapidly shuttled into a magnetically shielded region where the field is reduced to near zero and thus the name ZULF. The static magnetic field in the Hamiltonian is produced by small compensation coils inside the shield only to define a quantization axis for the purpose of detection and for lifting the degeneracies.

In CASPEr-ZULF, dark matter detection happens through the axion wind which is the last term in our Hamiltonian, D_{wind}. The time dependence of D_{wind} leads to an oscillatory modulation on the non-degenerate energy levels $m_F = \pm 1$, giving rise to more sidebands around the J-coupling doublet 2.11**C**. These extra sidebands will have an amplitude proportional to the modulation index g_{aNN}/ω_{DM} and thus by searching for these frequency modulations, dark matter can be detected in the non-resonant protocol of CASPEr-ZULF.

CASPEr-ZULF is of particular interest here as the sidebands induced here are not caused by gradients in the static field and are not due to dipole-dipole coupling. They are rather induced by a tiny static magnetic field that is applied for crucial reasons. However, if extra gradients show up in the applied static magnetic field, it might cause more splittings as we will see in our simulations and this is what we should be careful for and account for through calibration.

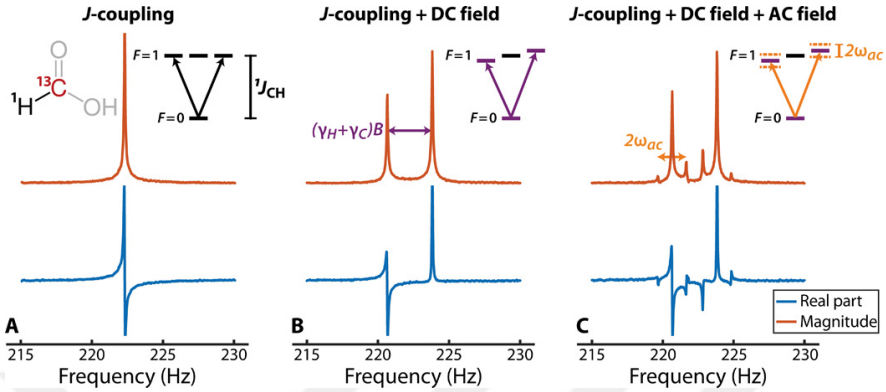

Figure 2.11: Energy levels and NMR spectra in a ZULF-NMR experiment in three conditions: **(A)** In the absence of magnetic field **(B)** In the presence of static magnetic field **(C)** In the presence of static and oscillating magnetic fields as reported in Ref. [2]. Reproduced from Garcon et al., *Science Advances*, 10.1126/sciadv.aax4539 (2019), AAAS.

2.10 Conclusion

In conclusion, this chapter has shown how nulcear magnetic resonance provides a rich and versatile framework for understanding spin dynamics, from the fundamental processes of polarization, coherent manipulation, relaxation and readout to the subtle effects introduced by magnetic field gradients and spin-spin interactions. By examining how gradients lead to inhomogeneous broadening, and through simulations demonstrating that such broadening can obscure signals arising from NOE, the importance of carefully disentangling environmental and interaction-driven contributions to NMR spectrum was highlighted. The discussion of the Overhauser effect and J-coupling further illustrated how inter-spin correlations shape both the dynamics and spectral structure of nuclear ensembles. Finally, the exploration of NMR-based dark matter experiments, such as CASPEr, emphasized how the same spin physics principles that enable chemical spectroscopy can be repurposed to probe fundamental questions about the strong CP problem and the nature of axions and ALPs.

Chapter 3

Optically Pumped Magnetometers (OPMs)

Optically-pumped magnetometers (OPMs) or atomic/optical magnetometers are quantum devices that measure extremely small magnetic fields by exploiting the magnetic sensitivity of the atom's electron spin. In OPMs, an alkali vapor cell (usually containing Rubidium or Cesium) is prepared so that the atomic spins become aligned or polarized using laser light, through the process of **optical pumping**. Once polarized, these spins precess in the presence of an external magnetic field at a frequency proportional to the field's strength. A second laser light detects the precession by monitoring changes in the atoms' optical properties through the process of **optical probing**. Because atomic spins respond very sensitively to tiny magnetic fields and because there is no need for cryogenic cooling, atomic magnetometers can achieve sensitivities comparable to or better than SQUIDs while remaining compact, low power and room-temperature devices. In this chapter, optical magnetometry will be explained with an overview of some of its applications in the field of dark matter detection and brain imaging.

3.1 Methodology

An optically pumped magnetometer consists of an alkali-atom vapor cell, optical pump and probe lasers, magnetic-field control coils and an optical detection system that converts atomic spin dynamics into a measurable signal.

3.1.1 Optical Pumping

Optical pumping is the process by which the atomic vapor inside the cell is prepared in a highly polarized spin state; it is where atoms in the bright state will absorb polarized light until they all relax to a dark state resulting in their polarization. It has many applications in atomic clocks, quantum optics, and magnetometry [53, 54]. In NMR, the spins were prepared or polarized using a strong static magnetic field. Instead, here alkali atoms will be polarized using circularly polarized laser light. The laser should be tuned near the D-line transitions of alkali atoms where it will selectively excite atoms from specific Zeeman sublevels following electric dipole selection rules. A right-circular polarization of light, σ_+ will target transitions following $\Delta m_F = +1$ selection rule, while a left-circular polarized light, σ_- will target transitions following $\Delta m_F = -1$ selection rule. Repeated absorption and spontaneous emission cycles transfer population towards magnetic fields that become dark for further excitation. When spins are in the dark state, they cannot absorb light and thus also cannot emit light anymore and this is how we know that spins are polarized. The redistribution of population creates a net angular momentum in the ensemble, enhancing its response to external magnetic fields. In optical pumping, the laser's stability and its polarization's purity are crucial for highly effective pumping that yields large polarization, long-lived coherence and a strong magneto-optical response.

3.1.2 Optical Probing

Optical probing is the stage at which the magnetometer reads out the spin state prepared by optical pumping, and it forms the bridge between atomic spin dynamics and the measured optical signal. To detect the spin dynamics created by both optical pumping and magnetic-field perturbations, a weak linearly-polarized probe laser passes through the polarized vapor. The probe is intentionally made weak, it perturbs the system minimally, allowing continuous measurement without significantly altering the system's population distribution, coherences and Larmor precession. The probe laser also should be kept perpendicular to the pump laser so that it doesn't get affected by the noise that results from the fluctuations in the intensity of the pump beam [55] The probe laser thus serves as a non-invasive optical readout of the atomic ensemble. Any magnetic-field-induced change in the atomic spin orientation is converted into a corresponding change in the transmitted probe beam which is detected using polarization optics and photodiodes. Therefore, the probing step converts the microscopic atomic response into a measurable macroscopic optical signal.

3.1.3 Atomic interactions

Atoms, being very sensitive sensors, interact with their surroundings through a combination of processes. **Light-atom interaction** encompasses the full suite through which electromagnetic radiation modifies atomic populations and coherences and in turn, through which atoms imprint their dynamics onto the optical field. A plane light wave will be altered as it traverses an atomic medium where there will be changes in the electric field amplitude (absorption), phase shift, polarization rotation and change in ellipticity [13].

Magneto-optical interaction represents a specialized subset of light-atom interactions that emerge when the atomic medium, in addition to being polarized by light, is also subjected to a magnetic field. As the linearly polarized beam enters the vapor cell, its components σ_+ and σ_- will each experience a different

complex refractive indices. The index of refraction is related to the phase shift and if a phase shift will take place, the polarization angle will rotate and this so called Faraday rotation is detected as a signal. The dynamics can be understood and studied using the evolution equations for the density matrix. To study that, we need the interaction Hamiltonian and the interactions that should be considered are the light-atom interaction, the magneto-optical interaction, the relaxation and repopulation dynamics of the atoms. The equations will then be studied in the steady-state condition and the solutions will tell us how the atoms affected the light [13].

The total Hamiltonian will contain the following terms:

1. **The unperturbed Hamiltonian** H_0 where the lower state's energy can be taken as zero and the excited state's Hamiltonian term is $\hbar\omega_0$ with ω_0 being the transition frequency.

2. **The light-atom interaction Hamiltonian** H_l which corresponds to the linearly polarized probe laser and its interaction with the atoms. The optical electric field will interact with the dipole operator as such: $H_l = - \boldsymbol{\varepsilon} \cdot \mathbf{d}$. The intensity of the optical field is determined by the Rabi frequency Ω_R, the greater Ω_R, the stronger the electric field amplitude and the faster the transition.

3. **The magnetic field interaction Hamiltonian** H_B determines how the sublevels will be affected by the external static magnetic field directed along z. The B-Field, lifts the degeneracy from the energy levels and the split of the energy levels is determined by the Larmor frequency Ω_L. The Hamiltonian $H_B = -\boldsymbol{\mu} \cdot \mathbf{B}$

The oscillating optical field will impose a problem due to its time dependence so to get rid of the time-dependence we go from the lab-frame to the rotating-frame by applying rotating wave approximation (RWA). This (RWA) will drop the fast-oscillating terms, leaving us with a static Hamiltonian.

The relaxation and repopulation dynamics of the atomic system do not show in the Hamiltonians but they should be accounted for. The relaxation represents two effects; the first one is that of the atoms exiting the light beam and the second one is that of the excited atoms in the upper state relaxing back to the ground state through spontaneous decay. When the light is turned off, the system is left to relax and during relaxation, the ground state population will go back to its equilibrium state thus repopulating the ground state [13].

The complete dynamics will be represented by the Liouville equation:

$$i\hbar\frac{d\tilde{\rho}}{dt} = \left[\tilde{H}, \tilde{\rho}\right] - \frac{i\hbar}{2}\left(\widehat{\Gamma}\tilde{\rho} + \tilde{\rho}\,\widehat{\Gamma}\right) + i\hbar\,\Lambda \tag{3.1}$$

where $\tilde{H}$ is the total Hamiltonian in the rotating frame, $\tilde{\rho}$ is the density matrix representing the system in the rotating frame, $\widehat{\Gamma}$ represents the relaxation matrix, and Λ represents the repopulation matrix. The Liouville equation is solved in the steady state and the solutions will appear in the observable signals.

3.2 The Cell

The vapor cell is the core of optically pumped magnetometers. It is the physical medium in which alkali atoms are prepared, polarized and perturbed. The cell defines the atomic density, relaxation dynamics, coherence lifetime and overall sensitivity of the device. The material composition of the vapor cell, its internal atmosphere, geometry and thermal conditions determine how well the atomic spins maintain orientation and how strongly the magnetic fields perturb them.

3.2.1 Why Alkali? Which Atom?

From its name, alkali vapor cells have inside them alkali atoms. Alkali atoms possess a single valence electron in their outermost shell, enabling efficient optical

pumping, large magnetic moments and strong magneto-optical effects. In alkali atoms, all the contribution of the angular momentum comes from the valence electron. In atoms with more electrons in their outermost shell, calculations become harder as in addition to all the couplings that should be studied and accounted for, the interaction between the electrons themselves should not be neglected or discrepancies will take place.

The choice of atom in the cell can be restricted by the availability of lasers at the appropriate wavelengths for example it can be significantly challenging and expensive to obtain a laser that would excite sodium atoms, making sodium atoms less popular in vapor cells. Sodium plays a unique role in remote magnetometry of the Earth's upper atmosphere. In the mesosphere, there is a naturally occurring layer of sodium atoms. This layer is illuminated with high power, narrow-linewidth lasers tuned at the sodium D_2 transition which is $\sim$ 589 nm [56]. In addition to the laser's availability, the vapor pressure and operating temperature of sodium make it less practical for tabletop OPMs [57].

In OPMs, usually Rubidium and Cesium are popular choices. Their D-line transitions (e.g. 795 nm and 780 nm for Rb, 852 nm and 894 nm for Cesium) [58, 59] fall in convenient laser-accessible regions. The vapor pressure of Cesium is higher at any given temperature than other alkali atoms which makes Cesium advantageous for unheated or near room temperature applications [60, 61]. Potassium has a much lower vapor pressure requiring higher operating temperatures, however, it has a set of distinctive physical advantages that make it highly attractive for applications that need enhanced sensitivity as potassium has extremely narrow magnetic-resonance line widths and very long coherence times [62, 63].

3.2.2 Spin Relaxation Mechanisms

As they depolarize and relax, the spins tend to reorient the atomic ground-state set by optical pumping, thus reducing the degree of alignment. The rate of relaxation of spins tells us about the coherence time of the atomic ensemble and dictates the signal amplitude, line width and thus the sensitivity of the device. In

alkali vapor cells, relaxation arises from several microscopic processes like spin-exchange collisions, spin-destruction collisions and wall collisions.

1. **Spin-Exchange Collisions:** It occurs when two alkali atoms collide and temporarily form an interaction allowing their electron spins to exchange angular momentum by swapping electronic spin states without changing the total spin of the ensemble. In spin-exchange collisions, the atoms can be redistributed among the Zeeman sublevels leading to a difference in the Larmor precession frequencies of the atoms and thus causing an effective broadening of magnetic-resonance lines. After the collision, the exchanged spin components begin to dephase relative to one another. [64]. This type of collision is the dominant contribution to the T_2 relaxation time and thus it limits the sensitivity. Spin-exchange relaxation mechanisms can be accounted for in the SERF regime (spin-exchange relaxation free) where the magnetic field is very low and all atoms precess at nearly the same frequency [65].

2. **Spin-Destruction Collisions:** Unlike spin-exchange collisions, spin-destruction collisions do not preserve the total spin of the alkali ensemble. These collisions take place during alkali-alkali collisions or alkali atoms colliding with other species like buffer gases and quenching gases. **Buffer gases**, like Helium, are added to alkali atoms in the vapor cell to suppress wall collisions and reduce atomic diffusion thus boosting coherence times. **Quenching gases**, like Nitrogen, are used to maintain strong optical pumping efficiency and minimize reabsorption effects that compete with spin orientation [60]. The spin-destruction collisions also broaden magnetic resonances. The cross-section of spin-destruction collisions is less than that of spin-exchange collisions and thus spin-destruction collision effect will be more pronounced when spin-exchange is reduced like in the SERF regime [66].

3. **Wall Collisions:** It happens when alkali atoms diffuse to the surface of the vapor cell and strikes the glass. The interaction with the wall destroys the spin polarization. After hitting the wall, the atom re-emerges with an

effectively randomized spin state. Wall collisions can be dominant over the other collisions unless suppressed. Suppressing wall coating can happen by adding buffer gas to the vapor cell or adding an anti-relaxation coating to the walls of the cell [64].

3.2.3 Buffer gas or AR coating?

To have an accurate measurement of the magnetic field using OPMs we need the atomic spins to precess longer and thus we aim for smaller relaxation rates which means extending the transverse relaxation time T_2. This can be done either by adding buffer gas to the cell or coating the cell with an anti-relaxation coating [67]. Both methods reduce wall collisions making the atoms undergo diffusive rather than ballistic motion.

There are some serious drawbacks of buffer gases and which is that they cause the atom to be spatially frozen making it more susceptible to magnetic-field gradients that lead to inhomogeneous broadening of the line shapes [60].

3.2.4 Heating the cell

Increasing the number of alkali atoms in the vapor cell will lead to a rise in magneto-optical detection as more sensors means more sensing. To increase the alkali atoms, we heat the cell as the alkali vapor density is directly affected by temperature. Increasing the density strengthens the absorption of the pump and probe beams. As the cell is heated and the number of atoms increases, collisional processes will also increase. It is crucial when heating the cell to have something that will counteract the collisions. As mentioned before, buffer gas or AR coating can be used for that aim. However, it is preferable to use a buffer gas with heat as the AR coating can only handle a temperature of $40°C$ which we need to exceed with some alkali atoms [68, 69].

3.3 Sensitivity

Sensitivity is one of the most important factors we have to account for when choosing the magnetometer. In NMR, sensitivity is limited by the tiny nuclear magnetic moment, the need for inductive detection which induces a very weak Faraday voltage and the noise temperature from the pickup coil. However, in OPMs, we have a much larger magnetic moment of electron spins and the magnetic field induced spin precession is converted into rotation or absorption of the beam so the noise caused by pickup coils is not present. In OPMs, the performance of the magnetometer is limited by quantum fluctuations caused by the alkali atoms and the photons from the probe beam. The sensitivity in OPMs, quantifies the smallest magnetic field the device can detect which is determined by the photon shot noise, the spin-projection noise and the quantum back action [66]. Combining these effects will give the fundamental sensitivity:

$$\delta B = \sqrt{\delta B_{SN}^2 + \delta B_{SPN}^2 + \delta B_{BA}^2} \tag{3.2}$$

3.3.1 Photon-Shot noise

The photon-shot noise δB_{SN} arises from the discrete nature of photons, having Poisson probability distribution in the probe beam, which leads to fluctuations in the detected optical power. When the shot noise limit is reached and all other sources of noise are negligible, the signal-to-noise ratio (SNR) increases. Here, the photon shot noise will be expressed in units of $\mathrm{T}/\sqrt{Hz}$ and it is related to the photon flux of the probe light Φ [60]:

$$\delta B_{SN} \propto \frac{1}{\sqrt{\Phi}} \tag{3.3}$$

3.3.2 Spin-Projection noise

The spin-projection noise, δB_{SPN}, originates from the intrinsic quantum uncertainty of the collective spin of the ensemble. Even if all the atoms are perfectly polarized along the z-axis, the transverse components will exhibit unavoidable fluctuations due to the Heisenberg uncertainty principle which is shown in equation (3.4) [60].

$$\Delta F_x \Delta F_y \geq \frac{\langle F_z \rangle}{2} \tag{3.4}$$

Spin-projection noise depends on the number of atoms in the ensemble N and the transverse relaxation time T_2 where:

$$\delta B_{SPN} \propto \frac{1}{\sqrt{N T_2}} \tag{3.5}$$

3.3.3 Back-Action noise

Back-action noise, δB_{BA}, originates from the measurement process itself. In quantum mechanics, we should disturb the system in order to measure it. Thus, to make a measurement on the atomic ensemble, the probe light that we send creates a fictitious magnetic field when it interacts with the electrons by shifting their energy levels and changing their precession frequency. This in turn, causes AC Stark shift or what we also call light shift [70]. Back-action is also related to the photon flux of the probe light Φ:

$$\delta B_{BA} \propto \sqrt{\Phi} \tag{3.6}$$

3.4 Gradients & Broadening

In OPMs, the sharpness of the magnetic resonance, expressed through the linewidth $\Gamma = 1/T_2$, determines how precisely the atomic ensemble responds to a driving field. A narrow resonance reflects long transverse coherence time T_2 and minimal dephasing, giving a sharp peak. Any mechanism that shortens T_2 increases the width of the resonance causing **broadening**. One important source of broadening is **magnetic-field gradients** which make atoms experience slightly different Larmor frequencies and accumulate spatially dependent phases. Anything that causes the ensemble to dephase faster, will broaden the spectrum. In NMR, broadening is caused by gradients that are generated by the coil, however, in OPMs, the broadening depends also on how atoms are moving through the field. For example diffusion determines how fast atoms are moving inside the gradients so if there is no buffer gas, the atoms have a fast diffusion, they move quickly through regions of different fields and they average the gradient over their motion thus reducing the broadening. But, if diffusion is slowed down, the atoms stay longer in a certain region and accumulate a phase determined by local fields which causes broadening [71]. The broadening due to gradients also depends on cell geometry, so a larger cell, even if it sounds better in terms of more atomic density, makes existing gradients more harmful because the atoms sample a larger variation of the field leading to stronger broadening [72]. The broadening does not also depend only on the magnitude of the gradient but also its direction relative to atomic motion and spin-polarization. A gradient parallel to the spin polarization axis changes the local Larmor frequency directly and therefore causes strong dephasing. In contrast, a gradient perpendicular to the polarization axis leads to reduced broadening.

3.5 Applications

Optically pumped magnetometers have evolved from laboratory instruments into versatile sensors capable of addressing problems across neuroscience, fundamental

physics and precision metrology. OPMs stand out as magnetic-field detection devices that, unlike SQUIDs, operate without cryogenic cooling. Among the most impactful application areas are magnetoencephalography (MEG) which are OPM wearable brain imaging devices with high spatial and temporal resolution [73, 74, 75]. Another application is the search for dark matter where OPMs function as exquisitely sensitive probes of tiny oscillating magnetic field signatures predicted in many axion-like models [76].

3.5.1 Magnetoencephalography (MEG)

MEG is a non-invasive neuro-imaging technique used to measure the tiny magnetic fields generated by electrical activity in the brain, offering a direct window into neuronal dynamics with very high temporal resolution. Like electroencephalography (EEG), MEG aims to track the timing and coordination of neural processes such as sensory perception [77], motor planning [78], language processing [79] and large scale oscillatory network activity in general. The primary and most established use for MEGs is in epilepsy [80]. It is also one of the most sensitive tools for identifying mild traumatic brain injury and post-concussive syndrome [81] and its sensitivity to oscillatory signatures makes it ideal for tracking diseases like Alzheimer [82] and Parkinson's [83]. In addition to that, eventhough this is still only research-oriented, MEG is becoming a powerful tool for understanding network biomarkers to understand Schizophrenia, Bipolar disorder, obsessive-compulsive disorder (OCD), major depression and autism [84, 85]. The key difference between EEG and MEG is that EEG measures electric potentials on the scalp while MEG measures the magnetic field produced by the same neuronal currents. Because electric fields are strongly distorted and attenuated by the skull's high electrical resistance, EEG signals become spatially blurred and are difficult to localize precisely. Since magnetic fields pass through tissues almost undisturbed, MEG has a significant spatial resolution over EEG [86]. Historically, MEG has relied on superconducting quantum interference devices (SQUIDs) but recently OPM-MEG is replacing SQUID-MEG for practical reasons which will be discussed in this section.

3.5.1.1 Origin of signals in the Brain

The magnetic fields measured by MEG ultimately arise from the motion of charged ions inside populations of specialized cells that receive, process and transmit information within the brain and throughout the body. These specialized cells are the nerve cells or neurons. The key ions involved in neural signaling are Sodium (Na^+), Potassium (K^+) and Chloride (Cl^-). When neurons in the brain undergo synaptic activity, the ions move across cell membranes, generating currents which then induce magnetic fields. The magnetic field produced by a single neuron is very weak to be measured outside the brain so what MEG measures is the macroscopic magnetic field induced by currents that are adding constructively which in turn are generated by tens of thousands of neurons that are firing simultaneously [86, 87].

3.5.1.2 MEG using SQUIDs

Historically, MEG has relied on superconducting quantum interference devices (SQUIDs) which offer excellent magnetic sensitivity but require cryogenic cooling usually with liquid Helium (4 K). The need for cryostats introduces several constraints:

1. The sensors must be kept several centimeters away from the scalp; 2-5 cm in adults and even more for children [86]. This distance drastically reduces spatial resolution.

2. The systems are heavy and fixed in shape, making them incompatible with head movement.

3. Cryogenic operation dramatically increases complexity and cost.

3.5.1.3 MEG using OPMs

OPM-MEG replaces cryogenic SQUIDs with room-temperature alkali vapor based magnetometers, allowing sensors to be placed directly on or only a few millimeters from the scalp [88] as shown in figue 3.1. This proximity increases spatial resolution and the OPMs are usually designed in a way that resembles a bicycle helmet which makes them compatible with head movement.

The magnetic fields generated by neural activity in the human brain are extraordinarily weak, typically in the range of 10-100 fT, which is about 10 billion times smaller than Earth's magnetic field ($\sim 50\ \mu$T). Even within a magnetically shielded room, residual static fields can remain at the level of tens to hundreds of nanotesla which is still many orders of magnitude larger than the neuromagnetic signals that an OPM must detect. Because these brain signals are so faint, the magnetometer must operate in a regime where the atomic spins respond with extreme coherence to very small magnetic perturbations. To achieve this, OPM-MEG systems actively *null* the DC magnetic field where specialized compensation coils generate a magnetic field equal in magnitude and opposite in direction to the residual field inside the room so that the net static field around each sesnor is brought as close to zero as possible [74]. The near-zero field is crucial not only for achieving the high spin coherence required for femtotesla sensitivity, but also for suppressing inhomogeneous broadening.

To null the DC, OPMs are first used for calibration by measuring the residual static field inside the room, where the atomic resonance frequency directly reports the local field. After knowing the magnitude and direction of the static fields inside the room, we can account for them using compensation coils. The precise field mapping and active cancellation suppress inhomogeneous broadening and ensure that all sensors operate in a uniform, high-coherence regime suitable for MEG [74].

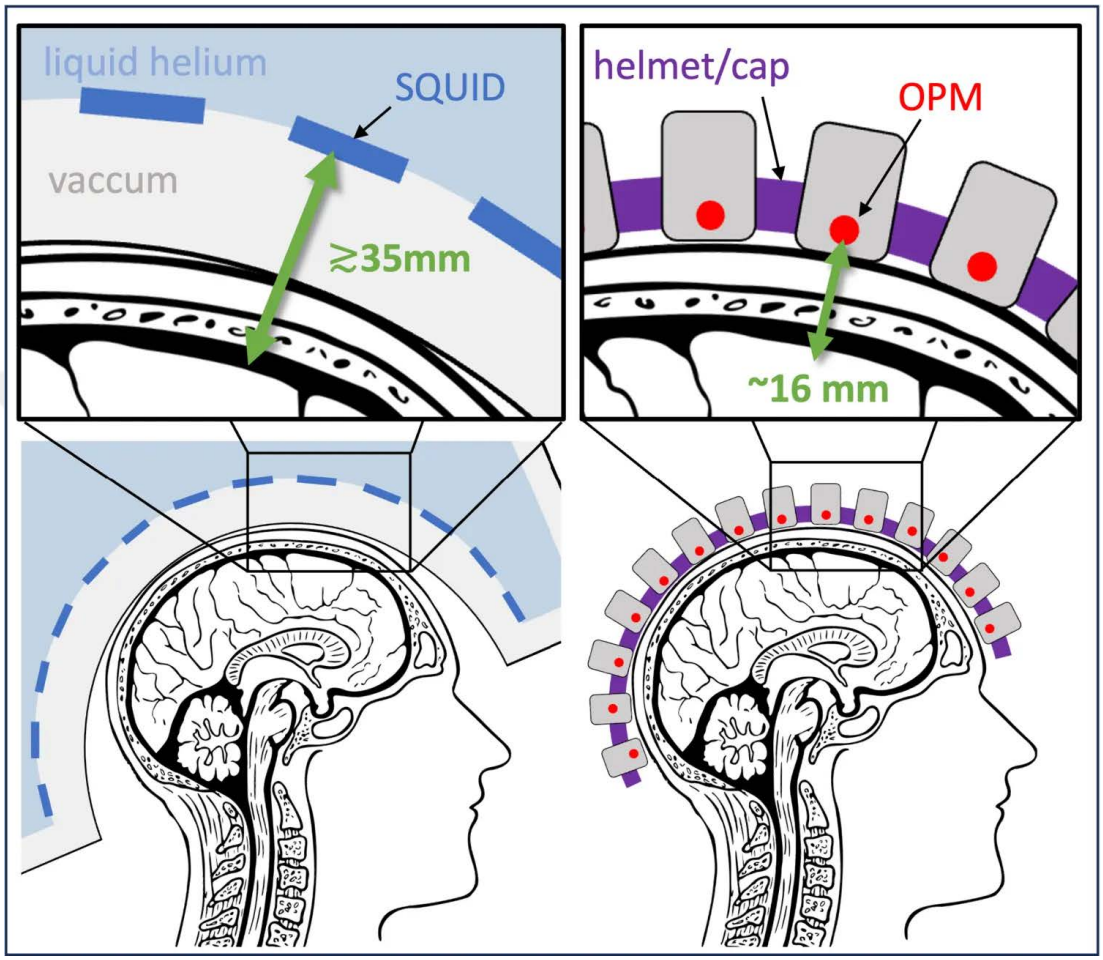

Figure 3.1: SQUID sesnor MEG (left) vs. on-scalp OPM sensor MEG (right). Image: Christoph Pfeiffer (head from public domain at Karolinska Institutet) [3]

3.5.2 Dark Matter

OPMs have also become central instruments in the search for dark matter and the **Global Network of Optical Magnetometers for Exotic physics searches** or GNOME is a prominent example [76, 89, 90]. GNOME is an international array of geographically distributed, high-sensitive OPMs designed to search for exotic fields.

The GNOME sensors are all optically pumped magnetometers that use alkali atoms (mostly Rb and Cs) to measure the spin precession upon the interaction of the alkali atoms with the laser beam and the exotic fields. The alkali atoms

are hosted in a glass cell which either has buffer gas to decrease spin-exchange collisions or has an anti-relaxation coating. The cell is also contained inside magnetic-field coils that control the homogeneous applied magnetic fields and also account for field gradients. Even though the cell will be sitting in a magnetic shield, external magnetic fields may still penetrate into the shield and introduce uncertainty in spin dynamics [90].

To increase the overall network sensitivity and to be able to probe various couplings of the exotic fields **comagnetometry** can be employed [91]. A comagnetometer is a special type of magnetometer in which two different spin species, typically an alkali atom (with electronic spin) and a noble gas (with nuclear spin) are polarized and measured inside the vapor cell [92, 93]. The brilliance behind comagnetometers is that because alkali atoms primarily probe electronic spin couplings while noble gas nuclei probe nuclear spin couplings, the combination allows the instrument to respond differently to ordinary magnetic fields versus exotic interactions. The two atomic species respond differently to ordinary magnetic fields but can be combined in a weighted way so that their magnetic responses cancel, making the device insensitive to ambient field fluctuations while remaining sensitive to exotic physics. This cancellation, however, only works if both species truly experience the same magnetic field but in a vapor cell the magnetic field is never perfectly uniform and instead contains spatial gradients. Because the two species differ in mass, diffusion constant and collision dynamics, they will average over the gradient differently, making their sampled magnetic fields nonidentical. This breaks the self-compensation or cancellation condition and produces residual signals that can mimic exotic fields. As a result, gradients cause inhomogeneous broadening, excess dephasing and false signals in comagnetometer outputs, problems that are especially severe and unwanted in GNOME.

3.6 Conclusion

Optically pumped magnetometers provide a powerful platform for precision magnetic-field sensing by exploiting the coherent interaction between resonant

light and atomic spin ensembles. Through careful control of optical pumping, probing, and cell composition and design, OPMs achieve long spin coherence high sensitivity. Understanding the roles of magnetic field gradients, line broadening and noise sources is essential for optimizing sensor performance and extracting reliable magnetic information. These principles form the basis for some of the most compelling applications of OPMs today, from non-invasive mapping of neural activity in magnetoencephalography to global, networked searches for exotic spin couplings in dark matter research efforts. Together, they demonstrate how atomic spin physics enables OPMs to remain at the forefront of modern quantum sensing technologies.

Chapter 4

NV Centers

So far spin dynamics in NMR and OPMs were studied, where one can come to the realization that the same core processes like spin preparation, perturbation, evolution and detection can be examined in different physical systems. Both platforms reveal how relaxation, dephasing and magnetic-field interactions shape the sensitivity of spin-based measurements.

Now the focus will be on a third class of quantum sensors which is nitrogen-vacancy centers in diamond or NV centers for short. NV centers stand out in some applications whose ingredients are nanoscale magnetometry and room temperature conditions. This chapter introduces the physics of NV centers, their spin dynamics, optical pumping, detection mechanisms and origins of inhomogeneous broadening. Sensing applications using NV centers will be discussed along with checking if NV centers are good candidates for MEG and dark matter detection. The conceptual framework built in the previous two chapters will naturally extend to this solid-state quantum platform, completing a unified picture of spin-based sensing across atomic, nuclear and solid-state systems.

4.1 Structure and Quantum Properties

The NV center in diamonds behaves as a solid-state atomic system whose quantum properties arise directly from its defect structure. Its optical transitions, charge states and spin configuration together determine how it can be initialized, manipulated and used as a sensor. In this section, the two charge states NV^0 and NV^- will be distinguished, then the spin-triplet structure which makes NV^- a powerful quantum sensor will be introduced and finally spin interactions will be discussed.

4.1.1 NV^0 vs. NV^-

The NV center is a point defect in diamond which consists of a substitutional Nitrogen atom adjacent to a missing Carbon atom and it inherits its quantum properties from the local reorganization of electronic orbitals around this defect.

To understand the NV center's charge states and spin properties, it is useful to consider first what happens when the Nitrogen atom is added and a Carbon site is left vacant. In a perfect diamond, each carbon atom contributes four valence electrons forming four covalent bonds. When a Carbon is removed, the three neighboring Carbon atoms each retain a dangling orbital, contributing one unpaired electron each. The added Nitrogen atom, which has five valence electrons, forms three covalent bonds with nearby Carbon atoms and leaves one additional dangling orbital directed toward the vacancy.

With a Nitrogen atom and a vacancy in the diamond, the number of electrons localized at the NV defect will be five in total; three from the neighboring Carbon atoms and two left from Nitrogen. The five electrons will make what is called the **neutral** NV^0 which will have an effective spin-1/2 ground state. The **negatively charged** NV^-, which is the one referred to as NV center, has an extra electron thus supporting a spin-triplet ground state.

NV^- is the charge state used for sensing [94] because it possesses a spin-1 triplet ground state with a large zero-field splitting meaning the states are separated even with no magnetic field and the splitting creates a natural frequency reference that shifts in the presence of magnetic or electric fields or strain or temperature which is exactly what one needs in a sensor. In addition to that, the NV^- with its $m_s = 0, +1, -1$ states, has a spin-dependent fluorescence and this difference in brightness produces optically detected magnetic resonance (ODMR) which allows us to see the spin state. Finally, the ability to optically polarize this charge state is essential for coherent control and high sensitivity measurements.

4.1.2 Electronic Spin Triplet

The NV center contains four atomic orbitals from the defect configuration and they are c_1, c_2 and c_3 corresponding to the three Carbon atoms and n corresponding to the Nitrogen. From the atomic orbitals, four molecular orbitals will be formed a_1, a_1', e_x and e_y, details can be found in [95, 96]. Each of these orbitals can hold two electrons and thus together they can hold a total of 8 electrons. With only 6 electrons for the NV center, and Hund's rule favoring the two electrons having parallel spins, we end up with a triplet state in the ground state. The uppercase labels A_1, A_2 and E seen in the level diagram in figure 4.1, which is adopted from proposed models in [97, 98], classify the symmetry type of an electronic state where A denotes a non-degenerate state and E a doubly-degenerate state. The subscripts 1 and 2 distinguish how the state behaves under certain mirror operations-details that are not needed here. The numbers on the left side of A and E indicate the spin multiplicity with three meaning a triplet state ($S = 1$), 1 meaning a singlet state ($S = 0$) and two meaning a doublet state ($S = 1/2$).

In the NV center, we have a spin-triplet ground state, a spin-triplet excited state and a singlet system involved in intersystem crossing as shown in the level diagram in figure 4.1. The spin-triplet spin basis of the ground and of the excited state are $|m_s = 0, \pm 1\rangle$. These three sublevels are non-degenerate even at zero

magnetic field because of spin-spin interactions within the defect. When exciting the population from the ground state to the excited state, upon relaxation, some of them undergo intersystem crossing (ISC) [99]. When ISC takes place, the population then decays to the singlet level with or without radiation, and finally it goes to the ground state.

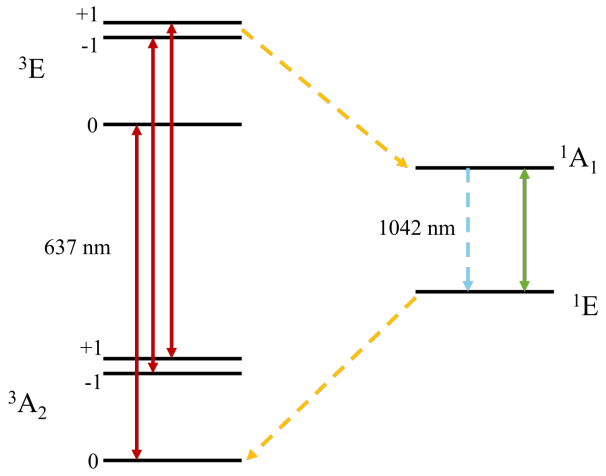

Figure 4.1: Level diagram for the NV center showing the spin conserving transitions between the ground state and the excited state (red arrosws) and the ISC (on the right) which shows non-radiative decay (dashed arrows).

4.1.3 Spin Interactions

The complete Hamiltonian of the NV center's ground state combines the electronic triplet spin, the nuclear spin of the host Nitrogen and their mutual interactions [66, 100]. The terms in the electronic Hamiltonian H_S contain the dominant zero-field splitting that separates $|m_s = 0\rangle$ from $|m_s = \pm 1\rangle$ with D = 2.87 GHz, the strain induced splitting that mixes the $|\pm 1\rangle$ manifold in non-ideal crystals, and the Zeeman interaction that shifts the energy levels in response to external magnetic fields. The terms in the hyperfine coupling Hamiltonian H_{SI} between the electron spin and the nitrogen nucleus contain first the parallel term which determines how the energies depend on their alignment along the NV axis, and the perpendicular term which describes the coupling in the transverse plane which leads to mixing and polarization transfer. Finally, the terms in the nuclear

Hamiltonian H_I contain the quadropole splitting of the $I = 1$ Nitrogen nucleus and its much weaker Zeeman response. These interactions are summarized visually in figure 4.2.

$$H = H_S + H_{SI} + H_I, \tag{4.1}$$

with

$$H_S = DS_z^2 + E\left(S_x^2 - S_y^2\right) + g_s\mu_B\,\mathbf{B}\cdot\mathbf{S}, \tag{4.2}$$

$$H_{SI} = A_\parallel S_z I_z + A_\perp\left(S_x I_x + S_y I_y\right), \tag{4.3}$$

$$H_I = PI_z^2 - g_I\mu_N\,\mathbf{B}\cdot\mathbf{I}. \tag{4.4}$$

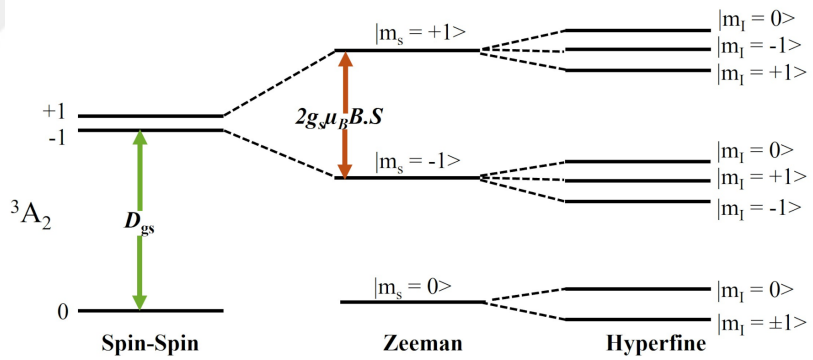

Figure 4.2: Ground-State Level diagram for the NV center showing the spin-spin interaction, Zeeman interaction, and the hyperfine interaction with Nitrogen's nucleus.

4.2 Spin Dynamics

The NV center combines the advantages of atomic-like coherence with the robustness and integrability of a crystalline host. NV centers can be initialized, coherently manipulated, and read out entirely optically at room temperature.

This remarkable capability arises from the wide band gap of diamond, which suppresses thermally activated charge carriers and isolates the NV electronic states from the surrounding lattice. Consequently, the NV spin retains stable energy levels and long coherence times, while spin-dependent optical transitions remain well defined even under ambient conditions.

In this section, the spin dynamics of NV centers in the framework of sensing, organized into preparation, perturbation, evolution and optical detection will be analyzed.

4.2.1 Initialization

As it was seen so far, the first step of using a system in sensing applications is to prepare that system in a well-defined state and then check if there will be any signal that will perturb that system from the defined state set by the experimenter. Preparing the NV center is done optically at room-temperature with visible light which makes it very convenient without any complicated Lasers or environments. The optical pumping mechanism in NV centers relies on the unique intersystem crossing (ISC) pathways, which selectively favors population transfer into the $m_s = 0$ ground state manifold.

Initially, the NV center will be in the ground state $^3A_2$ with sublevels $|m_s = 0\rangle$ and $|m_s = \pm 1\rangle$ being split by the zero-field splitting D = 2.87 GHz. NV centers can be polarized into the $m_s = 0$ state with green light (typically 532 nm), a mechanism without analogue in NMR and far more efficient than optical pumping in alkali vapors. Illuminating the NV center excites the electrons from the ground state to the excited state ^3E. Importantly, this is a **spin-conserving transition** as shown by the red arrows in the level diagram in figure 4.1. If all the decays from ^3E back to the $^3A_2$ were radiative and spin conserving, optical excitation would not produce polarization. Instead the NV would center between $^3A_2$ and ^3E without preferentially populating one spin sublevel.

The key feature of spin initialization is the presence of spin-dependent non-radiative decay channels via the singlet manifold and here is where the engine of spin polarization in NV centers, intersystem crossing (ISC), comes into place. ISC is a non-radiative transition between states of different spin multiplicities (triplet $\rightarrow$ singlet) which is forbidden by pure spin-selection rules but is allowed due to spin-orbit coupling [99]. The $|m_s = \pm 1\rangle$ sublevels in the excited state ^3E have a high probability of undergoing ISC to the singlet manifold (yellow arrow in figure 4.1) as shown by experiments [96, 98, 101]. The excited state $|m_s = 0\rangle$, which has a very small probability of ISC, decays radiatively back to the ground state $|m_s = 0\rangle$. The optical pumping cycle in NV centers is completed within a few microseconds which enables high repetition rate for sensing protocols.

The end of pumping is reached when the NV center fluoresces a strong red color. If the NV center is in the excited $|m_s = \pm 1\rangle$, it enters the ISC, undergoes non-radiative decay and yields a much weaker fluorescence. After continuous pumping, the measured fluorescence increases and reaches a steady high level which indicates that the NV center is mostly in $m_s = 0$ ground state.

4.2.2 Relaxation & Decoherence

The sensitivity of NV centers in diamonds to external fields, and the choice of sensing modality (section 4.2.3), are fundamentally limited and structured by their relaxation and decoherence processes. As in all spin systems, the NV electronic spin experiences energy relaxation, loss of phase coherence and inhomogeneous dephasing due to its solid-state environment. In what follows, the three characteristic relaxation times T_1, T_2 and T_2^* will be described along with their microscopic origins in the diamond host.

Longitudinal Relaxation Time T_1

The longitudinal relaxation time quantifies the rate at which the NV electronic spin returns to thermal equilibrium where a population redistribution $|m_s = \pm 1\rangle \rightarrow |m_s = 0\rangle$ sublevels occurs through energy exchange with the lattice. This

spin-lattice relaxation is driven primarily by phonon-mediated processes at the NV's zero-field splitting frequency ($\sim$ 2.87 GHz), as well as magnetic noise with spectral weight near this transition [102].

T_1 relaxation time, can be found by driving a microwave π pulse to transfer the system from the polarized $|0\rangle$ state to the $|+1\rangle$ state or the $|-1\rangle$ state. After some time t, a readout laser pulse is sent to measure the remaining population via fluorescence. The signal vs. time produces an exponentially decaying curve with the decay caused by T_1.

Coherence Time T_2

T_2 time is related to homogeneous spin dephasing which characterizes the decay of transverse coherence in the presence of dynamical decoupling or echo sequences such as Hahn echo. T_2 can be also referred to as the spin-spin relaxation time and that is because the spin-spin interactions are the dominant source of decoherence which is due to the coupling between the NV's electronic spin and other electronic spins in the lattice. Another source of decoherence is the coupling of the NV's electronic spins to the ^{13}C nuclear spin bath [4, 103].

The coherence time is measured using Hahn echo [16]. In a Hahn echo, after optical initialization, a $\pi/2$-pulse prepares the system in a coherent superposition, then the system is left to evolve for some time where there will be a phase accumulation. After which, a π-pulse is given to flip the spins and refocus them leaving them to evolve again for some time t. Then a final $\pi/2$-pulse is applied to convert coherence into population and a readout of fluorescence is done. From the resulting decaying signal, T_2 can be extracted.

Dephasing Time T_2^*

The inhomogeneous dephasing time T_2^* is the result of environment inhomogeneity that can originate from static magnetic field inhomogeneities and hyperfine interactions where the NV electronic spin can couple to the intrinsic nuclear spin of the Nitrogen atom or to the surrounding nuclear spin of ^{13}C [4].

The dephasing time T_2^* is measured using Ramsey interferometry [104]. In a Ramsey pulse sequence, a $\pi/2$-pulse is given to the initially polarized system to put it in a coherent superposition. The system is then left to evolve under the effects listed before. Then a second $\pi/2$-pulse is applied and readout of fluorescence is done. The fluorescence will oscillate between certain values, depending on the phase coherence between different states and the envelope of the oscillatory fluorescence will decay due to the dephasing effects. From the exponential decay we can know the value of T_2^*.

4.2.3 Sensing Protocols

Similar to alkali atoms in OPMs, NV centers magnetometry depends on measuring the transition frequency between energy levels whose response depends on external magnetic fields. The primary magnetic field measurement technique in NV centers is **optically detected magnetic resonance (ODMR)**, in which the spin-dependent photoluminescence (PL) is used to read out the population of the NV ground state sublevels. Where a population in the $|m_s = 0\rangle$ will result in a bright red luminescence, while a population in the $|m_s = \pm 1\rangle$ sublevels will give out a dimmer red luminescence. In NV magnetometry, the change in PL intensity will be our signal.

ODMR exists in several variants, two of which will be discussed here: continuous-wave (cw) and pulsed. Although they both rely on the same physical principle, they correspond to fundamentally different regimes of spin dynamics and, crucially, they access different physical quantities relevant for sensing.

ODMR enables magnetic field sensing because the NV's electronic ground state experiences a Zeeman shift $\Delta\omega = g_s \mu_B \, \mathbf{B} \cdot \mathbf{S}$ as shown in equation 4.2 and in figure 4.2. This shift modifies the microwave transition frequencies between $m_s = 0$ and $m_s = \pm 1$. Changes in this frequency which is induced by applied fields, biological samples or nanoscale magnetic objects, convert directly into shifts in the ODMR signal.

4.2.3.1 CW-ODMR

In the continuous-wave (cw) modality [105, 106, 107, 108], the NV is driven simultaneously and continuously by a green laser ($\sim$ 532 nm), a microwave (MW) field resonant with the ground state transitions and a readout laser as seen in figure 4.3a. Under continuous excitation, the NV reaches a steady state determined by the competition between optical pumping, MW-driven transitions, and relaxation processes. When the MW frequency ω_{MW} matches the energy splitting between $m_s = 0$ and $m_s = \pm 1$, population is coherently transferred to the darker sublevels, causing a drop in PL intensity. Scanning ω_{MW} across the resonance produces an ODMR spectrum, typically a Lorentzian dip, whose center frequency is sensitive to magnetic, electric and strain fields.

Cw-ODMR offers several major advantages with unbeatable experimental simplicity without the need of timing the electronics or pulse generation. However, in this modality, both the laser and the MW drive contribute to power broadening. Continuous laser illumination and MW driving increases the rate of ISC cycling and the rate of transitions, shortens the amount of time the spins can stay coherent thus shortening the coherence time T_2^* and broadens the linewidth. Because of this power broadening cw-ODMR typically has low sensitivity and it is not envisioned for sensitive magnetometry.

4.2.3.2 Pulsed ODMR

Pulsed-ODMR exploits the coherent evolution of the NV electronic spin. By separating optical pumping and microwave control into distinct temporal windows as shown in figures 4.3b and 4.3c, pulsed-ODMR avoids the power broadening inherent in cw-ODMR excitation and accesses the intrinsic coherence times T_1 and T_2, enabling orders of magnitude higher magnetic sensitivity [107].

A generic pulsed ODMR experiment proceeds in three steps:

1. Initialization: a short green pulse optically pumps the NV center to $|m_s = 0\rangle$

ground state.

2. Microwave-driven evolution: the green laser used for polarization is turned off and one or more MW pulses are applied to coherently manipulate the NV spin according to the desired pulse sequence. During this interval, the spin evolves freely or under controlled MW rotations without optical re-excitation.

3. Readout: A second short laser pulse converts the spin population into a PL signal.

Unlike cw-ODMR, in pulsed-ODMR power broadening doesn't impose a problem since by turning the laser off during the MW interrogation period, optical dephasing is removed which allows the linewidth to approach the intrinsic inhomogeneous dephasing limit $\Delta\nu = \frac{1}{\pi T_2^*}$ [107].

Pulsed-ODMR happens in two major forms which differ in the type of physical information they extract, the role of coherence and the relaxation times that govern the dynamics. The two major pulsed-ODMR modalities are:

1. **Single MW Pulse:** This is the simplest pulsed-ODMR experiment, it consists of a single MW pulse applied between polarization and readout as seen in figure 4.3b. When the MW frequency is resonant with the $|m_s = 0\rangle$ and $|m_s = \pm 1\rangle$ transition, the MW pulse rotates spin population into the darker states, reducing the observed PL. This method is ideal for determining resonance frequencies with high spectral resolution and performing spectroscopy without the broadening intrinsic to cw excitation.

2. **Ramsey Fringes:** Ramsey fringes [109] or the free-induction decay experiment or also referred to as the pump-probe experiment is a more complicated form of pulsed-ODMR which involves creating and detecting coherent superpositions. In this protocol, two $\pi/2$-pulses are applied between polarization and readout as can be seen in figure 4.3c. The first $\pi/2$-pulse places the NV spin into a coherent superposition. Then free evolution takes place

where the spin accumulates a phase proportional to the magnetic field. The second $\pi/2$-pulse converts this phase into a population difference which is detected through the final readout pulse. This protocol enables high sensitivity magnetometry, measurement of T_2^* via FID, sub-kHz frequency resolution and detection of extremely small magnetic fields via phase accumulation. Using Ramsey fringes, very long coherent evolution times can be reached, up to milliseconds [110, 111].

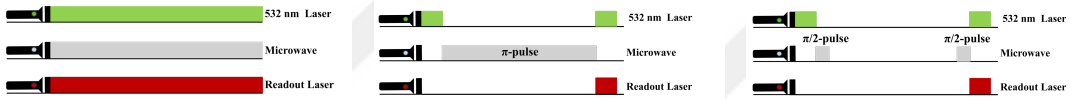

(a) (b) (c)

Figure 4.3: Comparison of sensing modalities: (a) CW-ODMR, (b) Single MW Pulsed-ODMR, and (c) Ramsey Pulsed-ODMR. Adapted from the schematic in Ref. [4].

4.2.4 Inhomogeneous Broadening

The sensing performance of NV center magnetometers is strongly influenced by the linewidth of their spin resonances which determines sensitivity, spectral resolution and the ability to detect small magnetic field variations. While homogeneous broadening caused by phonon interactions and spin-spin relaxation contribute to the intrinsic linewidth, many NV experiments are dominated by inhomogeneous broadening, which as we have seen in the previous chapters, is the spread of resonance frequencies arising from variations in the NV's local environment. These variations cause different NV centers to precess at slightly different frequencies, broadening their ODMR spectra and shortening the dephasing time T_2^*. Understanding the origins of this broadening and how to diagnose it is essential for optimizing NV-based sensing.

Inhomogeneous broadening originates from variations among the NV center's magnetic, electric and strain environment. In addition to effects arising from surrounding electronic and nuclear spin baths. Below, the mechanism of broadening

under each effect will be discussed.

1. **Magnetic Field Gradients:** This cause of inhomogeneous broadening has been already highlighted in previous chapters. It is where modifications to the Zeeman splitting will be induced by any spatial variation in the magnetic field along the NV axis. Sources include imperfectly aligned external fields, nearby magnetic impurities or nanoparticles [112, 113, 114]. These gradients are one of the most common sources of broadening in NV centers.

2. **Electric Field Gradients and Strain Variations:** The NV Hamiltonian, from equation 4.2 contains an electric field and strain sensitive term where E depends on the local transverse strain and electric fields [115, 113]. Strain gradients arise from crystal growth defects, thermal gradients and stress and mechanical deformation of the diamond.

3. **Electronic Spin Bath:** Nearby unpaired electronic spins, especially from substitutional nitrogen (P1 center) N_s^0 where S=1/2 [100], and other NV centers, create local magnetic fields. These dipolar fields broaden the resonance by producing random shifts in the NV transition frequency [116].

4. **Nuclear Spin Bath:** Diamonds typically contain $\sim 1.1\%$ ^{13}C nuclei, each with a nuclear spin $I = 1/2$. Their hyperfine fields shift the NV resonance frequency depending on their spatial configuration [117, 118]. Every NV center experiences a different arrangement of nearby ^{13}C spins, causing the resonance frequency to be distributed across the ensemble.

Although inhomogeneous broadening appears simply as a widened resonance or a rapid decay of coherence, its underlying can and should be identified by examining how the system responds to controlled changes in its environment. By systematically varying external parameters, one can distinguish the source of broadening as each class alters the NV resonances in a characteristic way but details about this will not be presented here.

4.3 Applications

NV centers in diamond have emerged as one of the most powerful platforms for quantum sensing [110, 111], enabling measurements of magnetic, electric, thermal and mechanical quantities with unprecedented spatial resolution and sensitivity. Their significance which stems from the room-temperature operation, their versatility, their scalability, long spin coherence times have led to what is widely regarded as a revolution in nanoscale magnetometry. This section reviews some quantum sensing applications and evaluates the extent to which NV centers provide an appropriate and effective sensing platform for each of them.

4.3.1 Biosensing

Because many biochemical processes involve unpaired electron spins, NV centers, with their significant previously mentioned properties, offer a fundamentally new way to study biology. The ability of NV centers to probe native biological structure and dynamics with nanometer spatial resolution is why they represent a revolutionary biosensing platform [119, 120].

The NV center senses its environment through magnetic dipole interactions between its electronic spin and external spins-either electron spins or nuclear spins-and through magnetic noise generated by nanoscale molecular motion. One of the examples of biosensing is Ferritin sensing. Ferritin is the primary iron-storage protein in the body and it contains a ferric (Fe^{3+}) mineral core. Abnormal ferritin or iron levels are clinically significant as they are associated with anemia, inflammation, neurodegenerative disease and disorders of iron metabolism. NV centers can detect ferritin because the unpaired electrons in the Fe^{3+} core generate nanoscale magnetic noise that modifies the NV spin relaxation time T_1 and coherence time T_2 [121]. When ferritin molecules are brought near the diamond surface, one can, by measuring the relaxation times, determine the presence and approximate concentration of ferritin at room-temperature and without invasive procedures.

NV centers also offer a fundamentally new approach to nuclear magnetic resonance at the nanoscale, enabling chemical and structural information to be obtained from volumes millions of times smaller than those accessible with conventional NMR coils. Traditional NMR requires macroscopic ensembles because inductive detection suffers from poor coupling to nuclear spins and large thermal noise, making it unsuitable for studying small biological samples, surface-bound molecules or single proteins. In contrast, the NV center directly detects the local magnetic fields generated by nearby nuclear spins through quantum-coherent phase accumulation, allowing high-sensitivity NMR spectroscopy within a sensing volume of only a few nanometers [122, 123, 124]. This ability is particularly valuable in biology, where many systems, such as lipid membranes, protein monolayers and cellular components, exist in quantities too small for conventional NMR but remain accessible to NV-based detection. By placing near-surface NV centers within nanometers of the sample, and by using Ramsey interferometry or Hahn echo sequences to filter nuclear precession frequencies, NV sensors can extract NMR spectra, measure relaxation times and probe chemical environments in real time. As a result, NV-based nanoscale NMR, without inductive coils and cryogenics represents a transformative tool bridging quantum sensing and biophysics.

4.3.2 Magnetoencephalography

Detection of magnetic fields generated by large neuronal populations in the brain using SQUID-MEG and OPM-MEG was discussed in section 3.5.1 and will be discussed here using NV centers in diamonds.

Despite their exceptional capabilities at the nanoscale, NV centers are generally considered unsuitable for magnetoencephalography, which requires detecting femtotesla-level magnetic fields which are millimeters, at best, away from the sensor [125]. In MEG, the sensor is separated from the brain by the skull, scalp, and intervening tissue, dramatically reducing the signal strength. Compared to SQUID-MEG or OPM-MEG, NV ensembles currently have lower magnetic

field sensitivity and struggle to achieve large area coverage required for whole-head imaging. For these reasons, while NV centers are excellent for micron and nanoscale neural measurements, they are still not competitive for macroscopic MEG applications.

4.3.3 Dark Matter

The detection of weakly interaction slim particles (WISPs), specifically axions and ALPs, as dark matter candidates was discussed in sections 2.9 and 3.5.2 where it was seen how NMR and OPMs can be used to search for fundamental physics and physics beyond the standard model.

WISPs, such as axions, ALPs and dark photons, are ultralight bosonic fields that behave as coherent, oscillatory backgrounds capable of driving spin-precession or modifying electromagnetic interactions in a continuous manner. WISPs' signals should couple to NV centers, however, WISPs typically generate extremely weak, globally coherent oscillatory fields that act uniformly over macroscopic volumes, whereas NV centers excel at detecting local magnetic fields in microscopic sensing volumes. With all these challenges, the search for WISPs using NV centers is still interesting for scientists and an active area of research. Theoretically, it was shown in [126] that axions and dark photons can be detected using NV centers focusing on axion-electron. Chigusa et al.'s proposal shows theoretically that NV centers could probe UBDM if one achieved extreme coherence times that is possible at cryogenic temperatures and operated large ensembles of up to 10^{20} NV centers. However, doing so requires levels of diamond engineering, optical control, noise suppression, thermal management and coherence preservation. Thus, while NV centers offer conceptual sensitivity to WISP dark matter, the experimental challenges make such searches unfeasible today.

In addition to WISPs, weakly interacting massive particle (WIMPs) form also a prominent class of dark matter candidates [127]. WIMPs are heavy particles (typically GeV-TeV masses) that do not generate coherent fields, instead, they interact with ordinary matter through rare, impulsive scattering events. While

WISPs manifest as perturbations to the Hamiltonian, WIMPs would produce localized, energy-deposition events due to elastic scattering with nuclei or interactions that cause transient lattice excitations [128, 129]. A WIMP scattering off a nucleus can produce a nanometer scale track of defects, vacancies or strain within the diamond lattice. NV centers are uniquely suited to detect such events because changes in the local strain, electric field, or spin environment modify the NV optical and spin properties in measurable ways.

NV centers thus provide a versatile solid-state platform whose unique combination of quantum sensitivity and nanoscale resolution may yet open new detection channels in future generations of dark-matter experiments.

4.4 Conclusion

NV center in diamonds provides a uniquely versatile solid-state spin system whose controllable initialization, coherent manipulation and spin-dependent optical readout enable a wide range of precision sensing modalities. By understanding the mechanisms of relaxation, decoherence and inhomogeneous broadening, one can optimize sensing protocols to extract magnetic, electric, thermal and structural information with exceptional spatial resolution. Although some challenges remain to use NV centers for very weak signals or exotic field sensing, the underlying principles highlighted in this chapter showed why NV centers continue to play a leading role in modern quantum metrology and serve as an essential bridge between fundamental spin dynamics and emerging technological applications.

Chapter 5

Conclusion & Outlook

This thesis has explored spin-based quantum sensing across three complementary platforms: nuclear magnetic resonance, optically pumped magnetometers, and nitrogen vacancy centers in diamonds. In each of these platforms, coherent control of spin systems was illustrated.

Beginning with NMR, the foundational spin dynamics that govern polarization, manipulation, relaxation, and detection were examined. Magnetic field gradients, inter-spin couplings,and the nuclear Overhauser effect were studied and their effect on the shape of spectral features was analyzed. Simulations presented in the thesis highlighted the subtleties of interpreting broadened line shapes and the challenges of distinguishing technical contributions from genuine spin-spin correlations.

Extending the principles presented in NMR to OPMs, it was shown how atomic ensembles can be polarized, probed and protected from decoherence, enabling extraordinary magnetic sensitivity in applications ranging from biomagnetism to global dark-matter searches. The thesis shows that OPMs exemplify how scalability into networks amplifies sensing power where MEG arrays leverage spatially dense OPM grids to reconstruct brain activity with high temporal resolution, while global networks like GNOME use long-term correlation across continents

to probe for dark matter or exotic events. These networked approaches highlight a central insight emerging from modern quantum sensing which is that the collective behavior of multiple sensors often reveals what no single sensor can detect alone.

Finally with NV centers, the solid-state domain was explored, again with the study of optical pumping, coherent microwave control, and spin-dependent fluorescence which allow nanoscale sensing. Relaxation, inhomogeneous broadening and environmental effects were shown along with their effect on the performance across different sensing modalities. As was done with NMR and OPMs, some of the emerging applications in NV centers was surveyed such as their application in biosensing to prospective WIMP and WISP searches while showing the challenges of implementing such a sensor for the detection of exotic fields or neural brain activity.

Taken together, these explorations show how quantum sensing forms a unified framework in which diverse spin systems, governed by similar dynamics can be tailored for precision magnetometry. Each platform carries inherent challenges like coherence limits in ensembles, technical noise in NMR and atomic vapors, strain and disorder in solid-state systems, but advances in materials, laser systems, and signal processing continue to expand their capabilities. Knowing the origins of noise and inhomogeneous broadening in the spectrum, one can work to achieve the highest sensitivity aspired in such systems.

Building on this unified perspective, the three platforms explored in this thesis can also be distinguished by the sensitivity and frequency regimes in which they operate most effectively. NMR-based sensors, leveraging long coherence times and narrow resonance line widths, achieve high sensitivity to weak magnetic fields, typically in the femtoTesla to picoTesla per root Hertz range, and are particularly well suited for low frequency measurements spanning the sub-Hz to kiloHertz regime. Optically pumped magnetometers, which exploit electronic spins together with optical polarization and readout, provide the highest magnetic sensitivities among room temperature sensors, commonly operating in the femtoTesla per root Hertz range for static and low frequency magnetic fields

with bandwidths extending up to the kiloHertz regime depending on the operating mode. NV center based sensors, while generally exhibiting lower absolute magnetic sensitivity, ranging from the nanoTesla to femtoTesla per root Hertz depending on whether single defects or ensembles are employed, offer access to a much broader frequency range extending from kiloHertz to gigaHertz. These complementary characteristics underscore that precision magnetometry is inherently platform-dependent, with each system optimized for a distinct balance between sensitivity, bandwidth, spatial resolution, and practical constraints.

Looking ahead, the techniques developed and analyzed in this thesis provide a foundation for further work in quantum sensing. The hope is to contribute to the next generation sensor architectures, with particular interest in advancing OPMs while focusing on the cell. The spin dynamics in the cell of OPMs have been enhanced by either adding buffer and quenching gases or by coating the cell. However, buffer gases cause the spins to be more susceptible to magnetic field gradients and the effect of coatings on the cell is still an active area of research. Therefore, I would like to explore a third option and see if it will affect the spin dynamics inside the cell, that is, by engineering the cell itself and seeing which shape and dimensions contribute best to the ensemble's dynamics. In the future, I aspire to contribute particularly to the development of sensors for biomedical applications, focusing on OPM-MEG and potentially hybrid systems that can hold the promise of non-invasive, high resolution mapping of neural activity, offering transformative possibilities for neuroscience and cognitive research.

As quantum technologies mature, their convergence with interdisciplinary fields will enable new platforms that combine sensitivity, scalability and accessibility. It is within this evolving landscape that I hope to pursue further research and contribute to technologies that deepen our understanding of both the physical world and the human brain.

Bibliography

[1] D. Aybas, J. Adam, E. Blumenthal, A. V. Gramolin, D. Johnson, A. Kleyheeg, S. Afach, J. W. Blanchard, G. P. Centers, A. Garcon, *et al.*, "Search for axionlike dark matter using solid-state nuclear magnetic resonance," *Physical Review Letters*, vol. 126, no. 14, p. 141802, 2021.

[2] A. Garcon, J. W. Blanchard, G. P. Centers, N. L. Figueroa, P. W. Graham, D. F. Jackson Kimball, S. Rajendran, A. O. Sushkov, Y. V. Stadnik, A. Wickenbrock, *et al.*, "Constraints on bosonic dark matter from ultralow-field nuclear magnetic resonance," *Science advances*, vol. 5, no. 10, p. eaax4539, 2019.

[3] Karolinska Institutet – NatMEG Core Facility, "What is meg?." `https://ki.se/en/research/research-infrastructure-and-environments/core-facilities-for-research/natmeg-core-facility/what-is-meg`.

[4] J. F. Barry, J. M. Schloss, E. Bauch, M. J. Turner, C. A. Hart, L. M. Pham, and R. L. Walsworth, "Sensitivity optimization for nv-diamond magnetometry," *Reviews of Modern Physics*, vol. 92, no. 1, p. 015004, 2020.

[5] J. J. Sakurai and J. Napolitano, *Modern quantum mechanics*. Cambridge University Press, 2020.

[6] A. Abragam, *The principles of nuclear magnetism*. No. 32, Oxford university press, 1961.

[7] R. H. Hashemi, W. G. Bradley, and C. J. Lisanti, *MRI: the basics*. Lippincott Williams & Wilkins, 2010.

[8] D. Budker and M. Romalis, "Optical magnetometry," *Nature physics*, vol. 3, no. 4, pp. 227–234, 2007.

[9] A. D. Ludlow, M. M. Boyd, J. Ye, E. Peik, and P. O. Schmidt, "Optical atomic clocks," *Reviews of Modern Physics*, vol. 87, no. 2, pp. 637–701, 2015.

[10] C. L. Degen, F. Reinhard, and P. Cappellaro, "Quantum sensing," *Reviews of modern physics*, vol. 89, no. 3, p. 035002, 2017.

[11] S. C. Benjamin, B. W. Lovett, and J. M. Smith, "Prospects for measurement-based quantum computing with solid state spins," *Laser & Photonics Reviews*, vol. 3, no. 6, pp. 556–574, 2009.

[12] M. Pompili, S. L. Hermans, S. Baier, H. K. Beukers, P. C. Humphreys, R. N. Schouten, R. F. Vermeulen, M. J. Tiggelman, L. dos Santos Martins, B. Dirkse, *et al.*, "Realization of a multinode quantum network of remote solid-state qubits," *Science*, vol. 372, no. 6539, pp. 259–264, 2021.

[13] M. Auzinsh, D. Budker, and S. Rochester, *Optically polarized atoms: understanding light-atom interactions*. Oxford University Press, 2010.

[14] F. Bloch, "Nuclear induction," *Physical review*, vol. 70, no. 7-8, p. 460, 1946.

[15] E. M. Purcell, H. C. Torrey, and R. V. Pound, "Resonance absorption by nuclear magnetic moments in a solid," *Physical review*, vol. 69, no. 1-2, p. 37, 1946.

[16] E. L. Hahn, "Spin echoes," *Physical review*, vol. 80, no. 4, p. 580, 1950.

[17] H. Kovacs, D. Moskau, and M. Spraul, "Cryogenically cooled probes—a leap in nmr technology," *Progress in Nuclear Magnetic Resonance Spectroscopy*, vol. 46, no. 2-3, pp. 131–155, 2005.

[18] M. H. Levitt, *Spin dynamics: basics of nuclear magnetic resonance*. John Wiley & Sons, 2008.

[19] J. Keeler, *Understanding NMR spectroscopy*. John Wiley & Sons, 2010.

[20] A. W. Overhauser, "Polarization of nuclei in metals," *Phys. Rev.*, vol. 92, pp. 411–415, Oct 1953.

[21] I. Solomon, "Relaxation processes in a system of two spins," *Phys. Rev.*, vol. 99, pp. 559–565, Jul 1955.

[22] C. P. Slichter, *Principles of magnetic resonance*, vol. 1. Springer Science & Business Media, 2013.

[23] D. Neuhaus, "Nuclear overhauser effect," *Encyclopedia of Magnetic Resonance*, 6 2011.

[24] D. Neuhaus and M. P. Williamson, *The Nuclear Overhauser Effect in Structural and Conformational Analysis*. VCH, 1st ed., 1989.

[25] D. Neuhaus, "Nuclear overhauser effect," *eMagRes*, 2007.

[26] C. Abel, S. Afach, N. J. Ayres, C. A. Baker, G. Ban, G. Bison, K. Bodek, V. Bondar, M. Burghoff, E. Chanel, *et al.*, "Measurement of the permanent electric dipole moment of the neutron," *Physical Review Letters*, vol. 124, no. 8, p. 081803, 2020.

[27] D. F. J. Kimball and K. van Bibber, *The Search for Ultralight Bosonic Dark Matter*. Springer, 2022.

[28] A. Zee, *Quantum field theory in a nutshell*, vol. 7. Princeton university press, 2010.

[29] J. E. Kim and G. Carosi, "Axions and the strong cp problem," *Reviews of Modern Physics*, vol. 82, no. 1, pp. 557–601, 2010.

[30] R. D. Peccei, "The strong cp problem and axions," in *Axions: Theory, Cosmology, and Experimental Searches*, pp. 3–17, Springer, 2008.

[31] R. D. Peccei and H. R. Quinn, "Constraints imposed by cp conservation in the presence of pseudoparticles," *Physical Review D*, vol. 16, no. 6, p. 1791, 1977.

[32] R. D. Peccei and H. R. Quinn, "Cp conservation in the presence of pseudoparticles," *Physical Review Letters*, vol. 38, no. 25, p. 1440, 1977.

[33] S. Weinberg, "A new light boson?," *Physical Review Letters*, vol. 40, no. 4, p. 223, 1978.

[34] F. Wilczek, "Problem of strong p and t invariance in the presence of instantons," *Physical Review Letters*, vol. 40, no. 5, p. 279, 1978.

[35] G. Bertone and D. Hooper, "History of dark matter," *Reviews of Modern Physics*, vol. 90, no. 4, p. 045002, 2018.

[36] F. Zwicky *et al.*, "The redshift of extragalactic nebulae," *Helv. Phys. Acta*, vol. 6, no. 110, p. 138, 1933.

[37] F. Zwicky, "On the masses of nebulae and of clusters of nebulae," *Astrophysical Journal, vol. 86, p. 217*, vol. 86, p. 217, 1937.

[38] V. C. Rubin and W. K. Ford Jr, "Rotation of the andromeda nebula from a spectroscopic survey of emission regions," *Astrophysical Journal, vol. 159, p. 379*, vol. 159, p. 379, 1970.

[39] V. C. Rubin, W. K. Ford Jr, and N. Thonnard, "Extended rotation curves of high-luminosity spiral galaxies. iv-systematic dynamical properties, sa through sc," *Astrophysical Journal, Part 2-Letters to the Editor, vol. 225, Nov. 1, 1978, p. L107-L111.*, vol. 225, pp. L107–L111, 1978.

[40] M. Roberts and A. Rots, "Comparison of rotation curves of different galaxy types," *Astronomy and Astrophysics, Vol. 26, p. 483-485 (1973)*, vol. 26, pp. 483–485, 1973.

[41] M. Bartelmann, "Gravitational lensing," *Classical and Quantum Gravity*, vol. 27, no. 23, p. 233001, 2010.

[42] D. Clowe, M. Bradač, A. H. Gonzalez, M. Markevitch, S. W. Randall, C. Jones, and D. Zaritsky, "A direct empirical proof of the existence of dark matter," *The Astrophysical Journal*, vol. 648, no. 2, p. L109, 2006.

[43] R. Durrer, *The cosmic microwave background*. Cambridge University Press, 2020.

[44] D. J. Eisenstein and W. Hu, "Baryonic features in the matter transfer function," *The Astrophysical Journal*, vol. 496, no. 2, p. 605, 1998.

[45] P. W. Graham and S. Rajendran, "New observables for direct detection of axion dark matter," *Physical Review D—Particles, Fields, Gravitation, and Cosmology*, vol. 88, no. 3, p. 035023, 2013.

[46] D. Budker, P. W. Graham, M. Ledbetter, S. Rajendran, and A. Sushkov, "Cosmic axion spin precession experiment (casper)," *arXiv preprint arXiv:1306.6089*, 2013.

[47] A. Garcon, D. Aybas, J. W. Blanchard, G. Centers, N. L. Figueroa, P. W. Graham, D. F. J. Kimball, S. Rajendran, M. G. Sendra, A. O. Sushkov, *et al.*, "The cosmic axion spin precession experiment (casper): a dark-matter search with nuclear magnetic resonance," *Quantum Science and Technology*, vol. 3, no. 1, p. 014008, 2017.

[48] P. W. Graham and S. Rajendran, "Axion dark matter detection with cold molecules," *Physical Review D—Particles, Fields, Gravitation, and Cosmology*, vol. 84, no. 5, p. 055013, 2011.

[49] D. Budker, P. W. Graham, M. Ledbetter, S. Rajendran, and A. O. Sushkov, "Proposal for a cosmic axion spin precession experiment (casper)," *Physical Review X*, vol. 4, no. 2, p. 021030, 2014.

[50] L.-S. Bouchard, A. Sushkov, D. Budker, J. Ford, and A. Lipton, "Nuclear-spin relaxation of pb 207 in ferroelectric powders," *Physical Review A—Atomic, Molecular, and Optical Physics*, vol. 77, no. 2, p. 022102, 2008.

[51] D. Robbes, "Highly sensitive magnetometers—a review," *Sensors and Actuators A: Physical*, vol. 129, no. 1-2, pp. 86–93, 2006.

[52] J. W. Blanchard and D. Budker, "Zero-to ultralow-field nmr," *Emagres*, pp. 1395–1410, 2007.

[53] W. Happer, Y.-Y. Jau, and T. Walker, *Optically pumped atoms*. John Wiley & Sons, 2010.

[54] A. Kastler, "Quelques suggestions concernant la production optique et la détection optique d'une inégalité de population des niveaux de quantifigation spatiale des atomes. application à l'expérience de stern et gerlach et à la résonance magnétique," *Journal de Physique et le Radium*, vol. 11, no. 6, pp. 255–265, 1950.

[55] I. Savukov and S. J. Seltzer, *Spin-exchange-relaxation-free (SERF) magnetometers*. Cambridge University Press, 2013.

[56] J. M. Higbie, S. M. Rochester, B. Patton, R. Holzlöhner, D. Bonaccini Calia, and D. Budker, "Magnetometry with mesospheric sodium," *Proceedings of the National Academy of Sciences*, vol. 108, no. 9, pp. 3522–3525, 2011.

[57] D. A. Steck, "Sodium d line data," *Report, Los Alamos National Laboratory, Los Alamos*, vol. 124, p. 74, 2000.

[58] D. A. Steck, "Rubidium 87 d line data," 2001.

[59] D. A. Steck, "Cesium d line data," 2003.

[60] A. Fabricant, I. Novikova, and G. Bison, "How to build a magnetometer with thermal atomic vapor: a tutorial," *New Journal of Physics*, vol. 25, no. 2, p. 025001, 2023.

[61] K. Jensen, M. A. Skarsfeldt, H. Stærkind, J. Arnbak, M. V. Balabas, S.-P. Olesen, B. H. Bentzen, and E. S. Polzik, "Magnetocardiography on an isolated animal heart with a room-temperature optically pumped magnetometer," *Scientific reports*, vol. 8, no. 1, p. 16218, 2018.

[62] K. Kamada, Y. Ito, and T. Kobayashi, "Human mcg measurements with a high-sensitivity potassium atomic magnetometer," *Physiological measurement*, vol. 33, no. 6, p. 1063, 2012.

[63] H. Dang, A. C. Maloof, and M. V. Romalis, "Ultrahigh sensitivity magnetic field and magnetization measurements with an atomic magnetometer," *Applied physics letters*, vol. 97, no. 15, 2010.

[64] S. J. Seltzer, *Developments in alkali-metal atomic magnetometry*. Princeton University, 2008.

[65] J. Li, W. Quan, B. Zhou, Z. Wang, J. Lu, Z. Hu, G. Liu, and J. Fang, "Serf atomic magnetometer–recent advances and applications: A review," *IEEE Sensors Journal*, vol. 18, no. 20, pp. 8198–8207, 2018.

[66] *Optical Magnetometry*. Cambridge University Press, 2013.

[67] H. Chi, W. Quan, J. Zhang, L. Zhao, and J. Fang, "Advances in anti-relaxation coatings of alkali-metal vapor cells," *Applied Surface Science*, vol. 501, p. 143897, 2020.

[68] W. Li, M. Balabas, X. Peng, S. Pustelny, A. Wickenbrock, H. Guo, and D. Budker, "Characterization of high-temperature performance of cesium vapor cells with anti-relaxation coating," *Journal of Applied Physics*, vol. 121, no. 6, 2017.

[69] Y. Gao, D. Ma, S. Jiang, Y. Ma, S. Li, K. Wang, and X. Xu, "A novel oven structure for improving temperature uniformity of vapor cell in atomic sensors," *Results in Physics*, vol. 47, p. 106339, 2023.

[70] M. Fleischhauer, A. Matsko, and M. Scully, "Quantum limit of optical magnetometry in the presence of ac stark shifts," *Physical Review A*, vol. 62, no. 1, p. 013808, 2000.

[71] G. Cates, D. White, T.-R. Chien, S. Schaefer, and W. Happer, "Spin relaxation in gases due to inhomogeneous static and oscillating magnetic fields," *Physical Review A*, vol. 38, no. 10, p. 5092, 1988.

[72] S. Pustelny, D. Jackson Kimball, S. Rochester, V. Yashchuk, and D. Budker, "Influence of magnetic-field inhomogeneity on nonlinear magneto-optical resonances," *Physical Review A—Atomic, Molecular, and Optical Physics*, vol. 74, no. 6, p. 063406, 2006.

[73] M. J. Brookes, J. Leggett, M. Rea, R. M. Hill, N. Holmes, E. Boto, and R. Bowtell, "Magnetoencephalography with optically pumped magnetometers (opm-meg): the next generation of functional neuroimaging," *Trends in Neurosciences*, vol. 45, no. 8, pp. 621–634, 2022.

[74] J. Iivanainen, R. Zetter, M. Grön, K. Hakkarainen, and L. Parkkonen, "On-scalp meg system utilizing an actively shielded array of optically-pumped magnetometers," *NeuroImage*, vol. 194, pp. 244–258, 2019.

[75] B. Zhao, L. Li, Y. Zhang, J. Tang, Y. Liu, and Y. Zhai, "Optically pumped magnetometers recent advances and applications in biomagnetism: A review," *IEEE Sensors Journal*, vol. 23, no. 17, pp. 18949–18962, 2023.

[76] S. Afach, D. Aybas Tumturk, H. Bekker, B. C. Buchler, D. Budker, K. Cervantes, A. Derevianko, J. Eby, N. L. Figueroa, R. Folman, *et al.*, "What can a gnome do? search targets for the global network of optical magnetometers for exotic physics searches," *Annalen der Physik*, vol. 536, no. 1, p. 2300083, 2024.

[77] J. Besle, O. Bertrand, and M.-H. Giard, "Electrophysiological (eeg, seeg, meg) evidence for multiple audiovisual interactions in the human auditory cortex," *Hearing research*, vol. 258, no. 1-2, pp. 143–151, 2009.

[78] L. I. Boon, V. J. Geraedts, A. Hillebrand, M. R. Tannemaat, M. F. Contarino, C. J. Stam, and H. W. Berendse, "A systematic review of meg-based studies in parkinson's disease: the motor system and beyond," *Human brain mapping*, vol. 40, no. 9, pp. 2827–2848, 2019.

[79] R. Salmelin, "Clinical neurophysiology of language: the meg approach," *Clinical Neurophysiology*, vol. 118, no. 2, pp. 237–254, 2007.

[80] M. Pedersen, D. F. Abbott, and G. D. Jackson, "Wearable opm-meg: A changing landscape for epilepsy," *Epilepsia*, vol. 63, no. 11, pp. 2745–2753, 2022.

[81] C. M. Allen, L. Halsey, G. Topcu, L. Rier, L. E. Gascoyne, J. W. Scadding, P. L. Furlong, B. T. Dunkley, R. das Nair, M. J. Brookes, *et al.*, "Magnetoencephalography abnormalities in adult mild traumatic brain injury: A systematic review," *NeuroImage: Clinical*, vol. 31, p. 102697, 2021.

[82] P. K. Mandal, A. Banerjee, M. Tripathi, and A. Sharma, "A comprehensive review of magnetoencephalography (meg) studies for brain functionality in healthy aging and alzheimer's disease (ad)," *Frontiers in computational neuroscience*, vol. 12, p. 60, 2018.

[83] C. Stam, "Use of magnetoencephalography (meg) to study functional brain networks in neurodegenerative disorders," *Journal of the neurological sciences*, vol. 289, no. 1-2, pp. 128–134, 2010.

[84] P. J. Uhlhaas, P. Liddle, D. E. Linden, A. C. Nobre, K. D. Singh, and J. Gross, "Magnetoencephalography as a tool in psychiatric research: current status and perspective," *Biological Psychiatry: Cognitive Neuroscience and Neuroimaging*, vol. 2, no. 3, pp. 235–244, 2017.

[85] M. Reite, P. Teale, and D. C. Rojas, "Magnetoencephalography: applications in psychiatry," *Biological psychiatry*, vol. 45, no. 12, pp. 1553–1563, 1999.

[86] R. Hill, *Design and fabrication for next generation Magnetoencephalography*. PhD thesis, University of Nottingham, 2020.

[87] J. Isakovic, I. Dobbs-Dixon, D. Chaudhury, and D. Mitrecic, "Modeling of inhomogeneous electromagnetic fields in the nervous system: a novel paradigm in understanding cell interactions, disease etiology and therapy," *Scientific reports*, vol. 8, no. 1, p. 12909, 2018.

[88] V. K. Shah and R. T. Wakai, "A compact, high performance atomic magnetometer for biomedical applications," *Physics in Medicine & Biology*, vol. 58, no. 22, p. 8153, 2013.

[89] S. Afach, B. C. Buchler, D. Budker, C. Dailey, A. Derevianko, V. Dumont, N. L. Figueroa, I. Gerhardt, Z. D. Grujić, H. Guo, *et al.*, "Search for topological defect dark matter with a global network of optical magnetometers," *Nature Physics*, vol. 17, no. 12, pp. 1396–1401, 2021.

[90] S. Pustelny, D. F. Jackson Kimball, C. Pankow, M. P. Ledbetter, P. Wlodarczyk, P. Wcislo, M. Pospelov, J. R. Smith, J. Read, W. Gawlik, *et al.*, "The global network of optical magnetometers for exotic physics (gnome): A novel scheme to search for physics beyond the standard model," *Annalen der Physik*, vol. 525, no. 8-9, pp. 659–670, 2013.

[91] H. Masia Roig *et al.*, "Search for exotic spin couplings with the global network of optical magnetometers for exotic physics searches," tech. rep., Faculty of Physics, Mathematics, and Computer Science, Johannes Gutenberg . . . , 2023.

[92] T. W. Kornack, R. K. Ghosh, and M. V. Romalis, "Nuclear spin gyroscope based on an atomic comagnetometer," *Physical review letters*, vol. 95, no. 23, p. 230801, 2005.

[93] W. Terrano and M. Romalis, "Comagnetometer probes of dark matter and new physics," *Quantum Science and Technology*, vol. 7, no. 1, p. 014001, 2021.

[94] R. Schirhagl, K. Chang, M. Loretz, and C. L. Degen, "Nitrogen-vacancy centers in diamond: nanoscale sensors for physics and biology," *Annual review of physical chemistry*, vol. 65, no. 1, pp. 83–105, 2014.

[95] L. Rogers, S. Armstrong, M. Sellars, and N. Manson, "Infrared emission of the nv centre in diamond: Zeeman and uniaxial stress studies," *New Journal of Physics*, vol. 10, no. 10, p. 103024, 2008.

[96] V. M. Acosta, *Optical magnetometry with nitrogen-vacancy centers in diamond*. University of California, Berkeley, 2011.

[97] Y. Ma, M. Rohlfing, and A. Gali, "Excited states of the negatively charged nitrogen-vacancy color center in diamond," *Physical Review B—Condensed Matter and Materials Physics*, vol. 81, no. 4, p. 041204, 2010.

[98] L. Robledo, L. Childress, H. Bernien, B. Hensen, P. F. Alkemade, and R. Hanson, "High-fidelity projective read-out of a solid-state spin quantum register," *Nature*, vol. 477, no. 7366, pp. 574–578, 2011.

[99] J. R. Maze, A. Gali, E. Togan, Y. Chu, A. Trifonov, E. Kaxiras, and M. D. Lukin, "Properties of nitrogen-vacancy centers in diamond: the group theoretic approach," *New Journal of Physics*, vol. 13, no. 2, p. 025025, 2011.

[100] J. Loubser and J. van Wyk, "Electron spin resonance in the study of diamond," *Reports on Progress in Physics*, vol. 41, no. 8, p. 1201, 1978.

[101] V. Acosta, E. Bauch, A. Jarmola, L. Zipp, M. Ledbetter, and D. Budker, "Broadband magnetometry by infrared-absorption detection of nitrogen-vacancy ensembles in diamond," *Applied Physics Letters*, vol. 97, no. 17, 2010.

[102] A. Jarmola, V. Acosta, K. Jensen, S. Chemerisov, and D. Budker, "Temperature-and magnetic-field-dependent longitudinal spin relaxation in nitrogen-vacancy ensembles in diamond," *Physical review letters*, vol. 108, no. 19, p. 197601, 2012.

[103] W. Gao, A. Imamoglu, H. Bernien, and R. Hanson, "Coherent manipulation, measurement and entanglement of individual solid-state spins using optical fields," *Nature Photonics*, vol. 9, no. 6, pp. 363–373, 2015.

[104] N. F. Ramsey, "A molecular beam resonance method with separated oscillating fields," *Phys. Rev.*, vol. 78, pp. 695–699, Jun 1950.

[105] G. Fuchs, V. Dobrovitski, R. Hanson, A. Batra, C. Weis, T. Schenkel, and D. Awschalom, "Excited-state spectroscopy using single spin manipulation in diamond," *Physical review letters*, vol. 101, no. 11, p. 117601, 2008.

[106] V. M. Acosta, E. Bauch, M. P. Ledbetter, C. Santori, K.-M. Fu, P. E. Barclay, R. G. Beausoleil, H. Linget, J. F. Roch, F. Treussart, *et al.*, "Diamonds with a high density of nitrogen-vacancy centers for magnetometry applications," *Physical Review B—Condensed Matter and Materials Physics*, vol. 80, no. 11, p. 115202, 2009.

[107] A. Dréau, M. Lesik, L. Rondin, P. Spinicelli, O. Arcizet, J.-F. Roch, and V. Jacques, "Avoiding power broadening in optically detected magnetic resonance of single nv defects for enhanced dc magnetic field sensitivity," *Physical Review B—Condensed Matter and Materials Physics*, vol. 84, no. 19, p. 195204, 2011.

[108] J. M. Schloss, J. F. Barry, M. J. Turner, and R. L. Walsworth, "Simultaneous broadband vector magnetometry using solid-state spins," *Physical Review Applied*, vol. 10, no. 3, p. 034044, 2018.

[109] N. F. Ramsey, "A molecular beam resonance method with separated oscillating fields," *Phys. Rev.*, vol. 78, pp. 695–699, Jun 1950.

[110] C. Degen, "Scanning magnetic field microscope with a diamond single-spin sensor," *Applied Physics Letters*, vol. 92, no. 24, 2008.

[111] J. M. Taylor, P. Cappellaro, L. Childress, L. Jiang, D. Budker, P. R. Hemmer, A. Yacoby, R. Walsworth, and M. D. Lukin, "High-sensitivity diamond magnetometer with nanoscale resolution," *Nature Physics*, vol. 4, no. 10, pp. 810–816, 2008.

[112] P. Kehayias, M. Mrózek, V. M. Acosta, A. Jarmola, D. Rudnicki, R. Folman, W. Gawlik, and D. Budker, "Microwave saturation spectroscopy of nitrogen-vacancy ensembles in diamond," *Physical Review B*, vol. 89, no. 24, p. 245202, 2014.

[113] P. Jamonneau, M. Lesik, J. Tetienne, I. Alvizu, L. Mayer, A. Dréau, S. Kosen, J.-F. Roch, S. Pezzagna, J. Meijer, *et al.*, "Competition between electric field and magnetic field noise in the decoherence of a single spin in diamond," *Physical Review B*, vol. 93, no. 2, p. 024305, 2016.

[114] Y. Rosenzweig, Y. Schlussel, and R. Folman, "Probing the origins of inhomogeneous broadening in nitrogen-vacancy centers with" doppler-free" type spectroscopy," *arXiv preprint arXiv:1807.09025*, 2018.

[115] F. Dolde, H. Fedder, M. W. Doherty, T. Nöbauer, F. Rempp, G. Balasubramanian, T. Wolf, F. Reinhard, L. C. Hollenberg, F. Jelezko, *et al.*,

"Electric-field sensing using single diamond spins," *Nature Physics*, vol. 7, no. 6, pp. 459–463, 2011.

[116] R. Hanson, V. Dobrovitski, A. Feiguin, O. Gywat, and D. Awschalom, "Coherent dynamics of a single spin interacting with an adjustable spin bath," *Science*, vol. 320, no. 5874, pp. 352–355, 2008.

[117] G. Balasubramanian, P. Neumann, D. Twitchen, M. Markham, R. Kolesov, N. Mizuochi, J. Isoya, J. Achard, J. Beck, J. Tissler, *et al.*, "Ultralong spin coherence time in isotopically engineered diamond," *Nature materials*, vol. 8, no. 5, pp. 383–387, 2009.

[118] A. Dréau, J.-R. Maze, M. Lesik, J.-F. Roch, and V. Jacques, "High-resolution spectroscopy of single nv defects coupled with nearby 13 c nuclear spins in diamond," *Physical Review B—Condensed Matter and Materials Physics*, vol. 85, no. 13, p. 134107, 2012.

[119] G. Balasubramanian, A. Lazariev, S. R. Arumugam, and D.-w. Duan, "Nitrogen-vacancy color center in diamond—emerging nanoscale applications in bioimaging and biosensing," *Current opinion in chemical biology*, vol. 20, pp. 69–77, 2014.

[120] T. Zhang, G. Pramanik, K. Zhang, M. Gulka, L. Wang, J. Jing, F. Xu, Z. Li, Q. Wei, P. Cigler, *et al.*, "Toward quantitative bio-sensing with nitrogen–vacancy center in diamond," *ACS sensors*, vol. 6, no. 6, pp. 2077–2107, 2021.

[121] A. Ermakova, G. Pramanik, J.-M. Cai, G. Algara-Siller, U. Kaiser, T. Weil, Y.-K. Tzeng, H.-C. Chang, L. McGuinness, M. B. Plenio, *et al.*, "Detection of a few metallo-protein molecules using color centers in nanodiamonds," *Nano letters*, vol. 13, no. 7, pp. 3305–3309, 2013.

[122] A. Boretti, L. Rosa, and S. Castelletto, "Towards single biomolecule imaging via optical nanoscale magnetic resonance imaging," *Small*, vol. 11, no. 34, pp. 4229–4236, 2015.

[123] D. Suter and F. Jelezko, "Single-spin magnetic resonance in the nitrogen-vacancy center of diamond," *Progress in nuclear magnetic resonance spectroscopy*, vol. 98, pp. 50–62, 2017.

[124] R. D. Allert, K. D. Briegel, and D. B. Bucher, "Advances in nano-and microscale nmr spectroscopy using diamond quantum sensors," *Chemical Communications*, vol. 58, no. 59, pp. 8165–8181, 2022.

[125] B. Bao, Y. Hua, R. Wang, and D. Li, "Quantum-based magnetic field sensors for biosensing," *Advanced Quantum Technologies*, vol. 6, no. 5, p. 2200146, 2023.

[126] S. Chigusa, M. Hazumi, E. D. Herbschleb, N. Mizuochi, and K. Nakayama, "Light dark matter search with nitrogen-vacancy centers in diamonds," *Journal of High Energy Physics*, vol. 2025, no. 3, pp. 1–19, 2025.

[127] L. Roszkowski, E. M. Sessolo, and S. Trojanowski, "Wimp dark matter candidates and searches—current status and future prospects," *Reports on Progress in Physics*, vol. 81, no. 6, p. 066201, 2018.

[128] S. Rajendran, N. Zobrist, A. O. Sushkov, R. Walsworth, and M. Lukin, "A method for directional detection of dark matter using spectroscopy of crystal defects," *Physical Review D*, vol. 96, no. 3, p. 035009, 2017.

[129] R. Ebadi, M. C. Marshall, D. F. Phillips, J. Cremer, T. Zhou, M. Titze, P. Kehayias, M. Saleh Ziabari, N. Delegan, S. Rajendran, *et al.*, "Directional detection of dark matter using solid-state quantum sensing," *AVS Quantum Science*, vol. 4, no. 4, 2022.